

Observational Insights on DBI K-essence Models Using Machine Learning and Bayesian Analysis

Samit Ganguly,^{1,2,*} Arijit Panda,^{3,†} Eduardo Guendelman,^{4,5,6,‡} Debashis Gangopadhyay,^{7,§} Abhijit Bhattacharyya,^{1,¶} and Goutam Manna^{a8,9,**}

¹Department of Physics, University of Calcutta, 92, A.P.C. Road, Kolkata-700009, India

²Department of Physics, Haldia Government College, Haldia, Purba Medinipur 721657, India

³Department of Physics, Raiganj University, Raiganj, Uttar Dinajpur, West Bengal, India, 733 134.

⁴Department of Physics, Ben-Gurion University of the Negev, Beer-Sheva, Israel

⁵Frankfurt Institute for Advanced Studies (FIAS),

Ruth-Moufang-Strasse 1, 60438 Frankfurt am Main, Germany.

⁶Bahamas Advanced Study Institute and Conferences, 4A Ocean Heights, Hill View Circle, Stella Maris, Long Island, The Bahamas.

⁷Department of Physics, School of Natural Sciences, Sister Nivedita University, DG 1/2, Action Area 1, Newtown, Kolkata 700156, India.

⁸Department of Physics, Prabhat Kumar College, Contai, Purba Medinipur 721404, India

⁹Institute of Astronomy, Space and Earth Science, Kolkata 700054, India

(Dated: June 9, 2025)

We present a comparative observational data analysis of two DBI-type k-essence scalar field models for late-time cosmic acceleration: one treats dark energy with standard matter, while the other unifies dark energy and dark matter within a single scalar field, each governed by distinct non-canonical Lagrangians. The background dynamics are formulated via modified Friedmann and scalar field equations, constrained by Pantheon+ SNe Ia, Hubble, and BAO data, using Bayesian inference (NUTS in NumPyro) and a neural network-based emulator for efficiency. Introducing a nuisance parameter μ_0 improves the robustness and interpretability of key cosmological parameters, particularly H_0 , r_d , and Ω_{d0} by absorbing residual systematics, thereby mitigating the Hubble tension. The deceleration parameter $q(z)$ is computed for both models, revealing key differences in cosmic acceleration history: Model I yields a present value $q_0^{Bayes} = -0.589$ or $q_0^{ML} = -0.559$ with transition redshift $z_{trans}^{Bayes} = 0.740$ or $z_{trans}^{ML} = 0.686$, closely aligning with Λ CDM predictions, while Model II shows a stronger present acceleration $q_0^{Bayes} = -0.893$ or $q_0^{ML} = -0.819$ but with a later transition at $z_{trans}^{Bayes} = 0.605$ or $z_{trans}^{ML} = 0.564$, indicating a steeper late time evolution. Based on χ^2 , χ^2_ν , AIC, and BIC statics, Model II performs worse than Model I despite its conceptual appeal. Finally, Symbolic regression (GPyLearn) is performed to reconstruct $\omega_{eff}(z)$. Our analysis shows that Model I is statistically favored across all metrics and offers a physically consistent alternative to Λ CDM, capable of addressing the Hubble tension.

PACS numbers: 04.20.-q, 04.50.Kd, 98.80.-k, 98.80.Es

Keywords: K-essence geometry, Early universe, Dark energy, Late-time acceleration, Observational data analysis

I. INTRODUCTION

The discovery that the expansion of the universe is not slowing down, as once expected, but instead accelerating, stands as one of the most profound revelations in modern cosmology [1–6]. This acceleration, first inferred from observations of distant Type Ia supernovae and later confirmed through measurements of the cosmic microwave background (CMB) and large-scale structure, challenges our understanding of gravity and the cosmic behavior of the universe. Within the framework of general relativity, elucidating this phenomenon necessitates the introduction of a new energy component, dark en-

ergy, which comprises about 70% of the universe's total energy density and exerts a negative pressure sufficient to produce cosmic acceleration.

The cosmological constant, albeit the most straightforward and well-examined option for dark energy, has significant theoretical difficulties. The standard cosmological model, the Λ CDM model, faces two main issues: fine-tuning and the cosmic coincidence problem. The cosmological constant Λ is a significant factor in the observed energy density, causing a 120-order difference in predictions and observations [7–11]. This significant disparity, known as the *cosmological constant problem*, has prompted the creation of many alternative theories.

Although the fine-tuning and cosmic coincidence problems pose enduring conceptual challenges in cosmology, they are not typically regarded as direct inconsistencies of the Λ CDM model. As a result, many researchers view them as theoretical concerns that may require reinterpretation rather than a fundamental modification of the prevailing paradigm [12, 13]. In contrast, the Hubble tension refers to the discrepancy between early and

* samitgphy07@gmail.com

† arijitpanda260195@gmail.com

‡ guendel@bgu.ac.il

§ debashis.g@snuniv.ac.in

¶ abhattacharyyacu@gmail.com

** goutammanna.pkc@gmail.com

^aCorresponding author

late-universe measurements of the Hubble constant H_0 . The early-universe estimate from CMB data, such as that from the Planck collaboration [14], is $H_0 \approx 67.4 \pm 0.5 \text{ km/s/Mpc}$, whereas late-universe direct local measurements, particularly from the SH0ES team [2, 15], yield $H_0 \approx 73.0 \pm 1.0 \text{ km/s/Mpc}$. This discrepancy has become a statistically significant observational issue. Its resolution likely necessitates new physics beyond the standard cosmological model. Proposed possibilities often include either altering the matter composition of the universe or revisiting the basic principles of gravity.

In this context, alternative theories of gravity have emerged as compelling avenues for understanding late-time acceleration. These theories aim to go beyond Einstein’s general relativity by introducing new degrees of freedom or modifying the behavior of gravity on cosmological scales, often without the need for a finely tuned cosmological constant. Among them, scalar field theories have received considerable attention [16–20], particularly those involving non-canonical kinetic terms that enrich the dynamics and offer greater flexibility in modeling the universe’s expansion history.

A significant category of these models is K-essence [10, 11, 21–48], wherein the Lagrangian exhibits a nonlinear dependence on both the scalar field and its kinetic term. The K-essence theory is a particular subclass of generalized scalar-tensor theories, situated within the context of Horndeski gravity [49–51]. It incorporates scalar fields with non-canonical kinetic parameters and offers a dynamic framework to elucidate cosmic acceleration while avoiding higher-order instabilities. K-essence, first suggested in relation to inflation, has since been modified to elucidate dark energy and the acceleration of the universe in its later stages. These models are especially appealing due to their capacity to demonstrate dynamical attractor solutions, allowing for a natural onset of acceleration without extreme sensitivity to initial conditions. Furthermore, K-essence permits a variable equation of state (ω), perhaps aligning more closely with data than a constant ω model. K-essence theory may also be used to examine unified dark energy and dust dark matter [52] in the realms of inflation and dark energy [53] within an alternate framework. The formation of K-essence dynamics without fine-tuning has been proven within the Two-Measures Field Theory (TMT) framework, which offers a natural basis for scalar field cosmology [54]. The detailed motivations, significance, applications, and various forms of the Lagrangian adapted to different cosmological scenarios within non-canonical theories such as K-essence can be found in [10, 11].

The impetus for observational insights into k-essence theory inside FLRW backgrounds arises from the need to elucidate the universe’s late-time acceleration beyond the cosmological constant. Examining the effects on the FLRW metric facilitates evaluating the theory’s coherence with empirical facts like supernovae, baryon acoustic oscillations, and the cosmic microwave background. As precision cosmology

advances, investigating k-essence offers an essential understanding of cosmic acceleration and evaluates its feasibility as a model for the evolving universe.

The Dirac-Born-Infeld (DBI) type non-canonical Lagrangian was originally inspired by attempts to resolve the problem of electron self-energy in classical electrodynamics [55]. Its characteristic square-root form naturally limits field gradients, preventing divergences and introducing nonlinear dynamics suitable for cosmology. In modern cosmological contexts, DBI-type k-essence has been applied in various scenarios, most notably in early universe inflation and late-time cosmic acceleration. In inflation, it enables slow-roll dynamics with distinctive signatures like large CMB non-Gaussianities, while in dark energy, its low sound speed affects structure formation compared to canonical models [33]. Additionally, DBI-type k-essence can also emerge from D-brane dynamics in wrapped string geometries [56–59].

From a physical standpoint, DBI-type k-essence models are particularly compelling because they maintain a subluminal and stable sound speed throughout the evolution of the universe. The sound speed in such models is given by $c_s^2 = \frac{\partial P}{\partial X} / \frac{\partial \rho}{\partial X}$, which, for DBI models, remains well-behaved and avoids instabilities like ghost modes or gradient instabilities that often afflict other dark energy scenarios with noncanonical kinetic terms [27, 33]. This makes DBI-inspired k-essence models both theoretically appealing and observationally viable, offering a rich phenomenology without sacrificing stability. Our focus will be on understanding how these models can drive cosmic acceleration while preserving desirable features such as dynamical attractors, theoretical consistency, and a well-behaved sound speed throughout cosmic history.

In this work, we present a comparative study of the Bayesian NUTS model [60] and machine learning techniques in cosmological data analysis [61] with two different DBI-type k-essence scalar field. In recent years, machine learning has become an emerging field for studying cosmological data due to its ability to model complex patterns and make accurate predictions from large datasets. Supervised learning algorithms, such as decision trees, support vector machines, and neural networks, are widely used for tasks ranging from classification to regression. In contrast, Bayesian methods—particularly those using advanced sampling techniques like the No-U-Turn Sampler (NUTS)—offer a principled probabilistic approach to data analysis. NUTS, an adaptive variant of Hamiltonian Monte Carlo (HMC) [62], allows for efficient exploration of high-dimensional posterior distributions without manual tuning, making it especially suited for scenarios where uncertainty estimation is crucial [63].

This paper is organized as follows: In Section II, we introduce the two DBI-type k-essence Lagrangians for scalar field models, derive their background dynamics, and formulate the essential evolution equations. Section III presents the observational framework and evolution equations in terms of redshift

distance (z), including luminosity distance, Hubble parameter, and energy density evolution, adapted for both models. In Section IV, we detail the methodology, combining Bayesian inference using NumPyro and machine learning-based surrogate modeling to fit the models to Pantheon+, Hubble, and BAO data, and reconstruct the EoS parameters using symbolic regression. Section V discusses the statistical comparison of the models using criteria such as χ^2 , AIC, and BIC, evaluates the deceleration parameter evolution, and assesses physical viability. We conclude in Section VI by summarizing our results and their implications for k-essence cosmology and dark sector modeling.

II. DBI-TYPE K-ESSENCE LAGRANGIAN AND DERIVATION OF ESSENTIAL DYNAMICS

K-essence theories are scalar field models characterized by a Lagrangian that depends nonlinearly on the kinetic term $X = \partial_\mu \phi \partial^\mu \phi$, where ϕ is the k-essence scalar field. Unlike canonical scalar field theories where the kinetic term appears linearly, k-essence allows for a richer dynamical structure, making it suitable for modeling both early and late-time cosmic acceleration [27, 31–33, 64]. Among the many forms of k-essence, one particularly well-motivated example is the DBI-type k-essence model. In this work, we explore two distinct classes of k-essence scalar field models within the framework of the DBI-type Lagrangian.

Model-1: A general DBI-type action is given by [27, 64] :

$$S_{DBI} = - \int d^4x \sqrt{-g} \left[f(\phi) \sqrt{1 - \frac{2X}{f(\phi)}} - f(\phi) + V(\phi) \right] \quad (1)$$

Here $f(\phi)$ is the tension/wrap factor, which may be called “*tension scalar*”, and $V(\phi)$ is the potential. Note that here we assume the scalar field to be homogeneous, i.e. $\phi(r, t) \equiv \phi(t)$, since k-essence geometry permits us to make this type of choice [39, 40]. Now the variation of the above action with respect to the scalar field ϕ and the gravitational metric in the usual FLRW background with zero curvature leads to the scalar field equation of motion (EoM) and the energy-momentum tensor ($T_{\nu(\phi)}^\mu$). We can express them respectively as :

$$\ddot{\phi} - \frac{3f'(\phi)}{2f(\phi)} \dot{\phi}^2 + f'(\phi) + \frac{3H}{\gamma^2} \dot{\phi} + \frac{1}{\gamma^3} [V'(\phi) - f'(\phi)] = 0$$

and

$$T_{\nu(\phi)}^\mu = (\rho_\phi + P_\phi) u^\mu u_\nu - P_\phi \delta_\nu^\mu, \quad (3)$$

with

$$u_\mu = \frac{\partial_\mu \phi}{\sqrt{2X}} \quad ; \quad u_\mu u^\mu = 1. \quad (4)$$

Here, in Eq. (2) ‘dash’ denotes the derivative with respect to the scalar field ϕ and ‘dot’ denotes the derivative with respect to coordinate time, t and (3) ρ_ϕ and P_ϕ denote the energy density and pressure of the scalar field sector, respectively. H ($= \frac{\dot{a}}{a}$) is the Hubble parameter, $a \equiv a(t)$ is the scale factor. We can write the total energy density and pressure as [64]:

$$\begin{aligned} \rho &= \rho_\phi = (\gamma - 1)f(\phi) + V(\phi); \\ P &= P_\phi = \left(\frac{\gamma - 1}{\gamma}\right)f(\phi) - V(\phi) \end{aligned} \quad (5)$$

where the factor γ can be mapped with the relativistic Lorentz factor [64]:

$$\gamma = \frac{1}{\sqrt{1 - \frac{2X}{f(\phi)}}}. \quad (6)$$

Note that here the Lorentz factor depends on both the kinetic term ($2X$) as well as the tension scalar ($f(\phi)$). This highlights the non-trivial coupling between the scalar field’s dynamics and the effective geometry. In this geometry, the kinetic term governs the field’s energy density, while the tension scalar modulates the maximum attainable speed, thereby determining how relativistic effects can affect the evolution of the universe. The statement can be interpreted as follows: as the kinetic term increases, the kinetic energy of the field increases, pushing γ towards a larger value, but the tension scalar ($f(\phi)$) sets an upper limit to the kinetic term ($2X$). In particular, for the square root in the Lorentz factor in the denominator to remain real and positive, the quantity $\frac{2X}{f(\phi)} < 1$ must hold. Therefore, $f(\phi)$ effectively controls how fast the field can evolve, analogous to how the speed of light limits the velocity of particles in special relativity.

Now, to characterize the evolution of this scalar field, we introduce the *equation of state parameter* and sound speed, defined as:

$$\begin{aligned} \omega_\phi &= \frac{P_\phi}{\rho_\phi} = \frac{\left(\frac{\gamma - 1}{\gamma}\right)f(\phi) - V(\phi)}{(\gamma - 1)f(\phi) + V(\phi)} \equiv \omega_{dark} \\ c_s^2 &= \frac{\frac{\partial P}{\partial \rho}}{\frac{\partial \rho}{\partial X}} = \frac{1}{\gamma^2} \end{aligned} \quad (7)$$

Note that here the Lorentz-like factor γ governs the behavior of the field, tightly coupling the equation of state parameter ω_ϕ and the sound speed c_s^2 . Specifically, when $\gamma \gg 1$, Lorentz factor-dependent term (2) dominates over the potential term ($V(\phi)$) leads to $\omega_\phi \rightarrow 0$ and $c_s^2 \rightarrow 0$, which mimics cold dark matter. Conversely, in the limit $\gamma \rightarrow 1$, the potential term dominates, leading to $\omega_\phi \approx -1$ and $c_s^2 \approx 1$, characteristic of dark energy. While this dual behavior

suggests the model could interpolate between dark matter and dark energy phases, there are critical limitations that obstruct a successful unification. The transition between these regimes depends sensitively on the evolution of $\dot{\phi}$ and the specific functional form of the tension scalar $f(\phi)$, which often imposes conflicting requirements.

On the other hand, $2X > f(\phi)$, then we can not find any smooth transition from the dark matter-like regime to a dark energy-like phase, where γ becomes ill-defined, resulting in a breakdown of the theory. These issues arise from the inherent competition between the kinetic energy and the tension, which prevents a coherent and physically viable evolution across cosmic time.

Therefore, although this DBI-type Lagrangian (1) can effectively model dark energy and dark matter in isolation, it lacks the internal consistency and dynamical flexibility needed to serve as a unified description of the entire dark sector. In this context, we redefine the equation of state parameter definition in Eq.(7), ω_ϕ to ω_{dark} , which now exclusively describes the dark energy sector, since Eq. (1) is incapable of simultaneously representing both dark matter and dark energy inside a single Lagrangian.

Furthermore, we observe that from Eq. (7), sound speed (c_s) is inversely related to the Lorentz factor (γ), which may suggest the following scenarios: If the sound speed (c_s) is less than 1 (and therefore $\gamma > 1$), it signifies that the scalar field exhibits relativistic behavior. This slows down the propagation of scalar perturbations, amplifies non-linear effects, affects structure creation, and may produce detectable signatures in the CMB and large-scale structure, rendering it a crucial signature of non-canonical theories such as K-essence or DBI cosmology.

K-essence models have been proposed as a compelling framework for explaining the accelerated expansion of the universe [21, 22]. The factors for this accelerated expansion include one of the possibilities is dark energy, which is effectively characterized by a non-canonical scalar field, whose dynamics may be governed by the action presented in Eq. (1). This scalar field naturally exhibits the negative pressure required for late-time cosmic acceleration, thereby mimicking the behavior of dark energy. Consequently, to achieve a unified cosmological description, it is essential to include a separate matter sector alongside the scalar field. This additional sector accounts for the distribution and clustering of matter, effectively representing the role of dark matter in structure formation. Therefore, the scalar field (1) contributes primarily to the late-time acceleration, whereas the standard pressure-less matter component accounts for structure formation in the early universe. Hence, the total action is given by:

$$S = S_{DBI} + S_m \quad (8)$$

with S_m being the matter sector action, which is expressed in terms of the matter Lagrangian \mathcal{L}_m as: $S_m = \int d^4x \sqrt{-g} \mathcal{L}_m$,

corresponding energy-momentum tensor is: $T_\nu^{\mu(m)} = (\rho_m + P_m)u^\mu u_\nu - P_m \delta_\nu^\mu$. Consequently, we define an effective equation of state parameter (ω_{eff}) in relation to the total Lagrangian $\mathcal{L} = \mathcal{L}_m + \mathcal{L}_\phi$ later in Eq. (25). Henceforth, all our subsequent calculations and analyses for Model I are based on the total action defined in Eq. (8), which encapsulates the contributions from both the k-essence scalar field and the matter component in a unified framework.

Model-2: An alternative form of the DBI-type scalar field Lagrangian [32, 65, 66] can be expressed as:

$$S_{DBI} = - \int d^4x \sqrt{-g} [V(\phi) \sqrt{1 - 2X}] \quad (9)$$

This specific form of the action is often referred to as a tachyon-type scalar field model, inspired by developments in string theory, where tachyon condensates emerge in the context of unstable D-brane systems [66, 67]. The non-canonical square-root kinetic structure leads to a rich dynamical behavior that interpolates between matter-like and cosmological-constant-like evolution, making it a compelling candidate for modeling both early-time inflation and late-time cosmic acceleration within a unified framework [27, 31, 32, 46, 65, 68].

Following a similar procedure as before, we vary the action (9) concerning the scalar field ϕ and the gravitational metric to derive the corresponding EoM and the energy density of the scalar field. In a spatially flat FLRW background, these expressions take the form:

$$\ddot{\phi} + 3 \frac{H}{\gamma^2} \dot{\phi} + \frac{V'(\phi)}{V(\phi)} \frac{1}{\gamma^2} = 0 \quad (10)$$

with

$$\rho_\phi = 2X \mathcal{L}_\mathcal{X} - \mathcal{L} = \frac{V(\phi)}{\sqrt{1 - 2X}} \quad (11)$$

where $\mathcal{L} = -V(\phi)\sqrt{1 - 2X}$ and $\gamma = \frac{1}{\sqrt{1 - 2X}}$. Notably, the Lorentz factor (γ) is only dependent on the kinetic factor; it remains positive and real when $2X < 1$.

The remarkable feature of this stress-energy tensor is that it can be broken into two components, with one behaving as a pressure-less dust (ρ_m) and the other having negative pressure (ρ_d) [32], therefore we can write them as:

$$\rho_\phi = \rho_m + \rho_d ; P_\phi = P_m + P_d \quad (12)$$

where,

$$\begin{aligned} \rho_m &= \frac{V(\phi)2X}{\sqrt{1 - 2X}} ; P_m = 0; \\ \rho_d &= V(\phi)\sqrt{1 - 2X} ; P_d = -\rho_d \end{aligned} \quad (13)$$

For this Model (9), ω_{eff} and c_s^2 can be expressed as:

$$\begin{aligned}\omega_{eff} &= \frac{P_\phi}{\rho_\phi} = -(1 - 2X) \\ c_s^2 &= \frac{\frac{\partial P}{\partial X}}{\frac{\partial \rho}{\partial X}} = \frac{1}{\gamma^2} = 1 - 2X\end{aligned}\quad (14)$$

The important point is that although the energy density and pressure (13) depend on the potential $V(\phi)$ but the effective equation of state parameter and sound speed (14) only depend on the kinetic term X . It highlights that the dynamical behavior of the system, whether it mimics dark energy or matter, emerges purely from the kinetic part of the scalar field rather than its potential energy configuration. It is the transition of ω_{eff} purely through variations in X , which enables the model to unify the dark sector, interpolating between dark energy and dark matter behaviors dynamically, *without needing separate fields or potentials*. So, we may say that the DBI-type k-essence action (9) can provide a unified theory of dark matter and dark energy without considering the Λ CDM model. It can also be said that this type of DBI action can explain the early universe as well as the late-time accelerated present universe. At this point, it should be mentioned that the Planck collaborations' results [14, 69–72] observationally investigated measures of different cosmological parameters and their constraints via the DBI-type action in k-essence geometry.

It is important to note that Model I in Eq. (1) and Model II in Eq. (9) represent two distinct classes of DBI-type k-essence Lagrangian that yield the correct equation of motions mentioned in Eqs. (2) and (10), respectively. The primary distinction between the models lies in the functional structure and dynamical role of the scalar field kinetic term and potential. While for Model I both $f(\phi)$ and $V(\phi)$ explicitly influence the dynamics, however, in Model II, the Lagrangian depends only on the potential coupled directly to the DBI kinetic term. It should be noted that although there is a broad freedom in choosing the functional form of $f(\phi)$ and $V(\phi)$, we adopt a specific choice that satisfies the necessary stability condition, which enables us to carry out consistent observational data analysis.

We will now proceed to data analysis with PAN-THEON+SHOES [74, 75], *Hubble* [76–88] and BAO data [89–92]. The Pantheon+SHOES dataset combines the Pantheon compilation of Type Ia supernovae with the SHOES team's precise local measurements of the Hubble constant. It provides one of the most comprehensive and high-precision datasets for constraining cosmological models and studying the universe's expansion history. The Hubble dataset consists of direct measurements of the Hubble parameter $H(z)$ at various redshifts, obtained from cosmic chronometers and BAO (Baryon Acoustic Oscillation) observations. It provides crucial information about the expansion rate of the universe over time,

helping to constrain dark energy and cosmological models. The BAO dataset captures the imprint of early-universe sound waves in the large-scale structure of galaxies. It serves as a standard ruler to measure cosmic distances and expansion history, providing strong constraints on dark energy and cosmological parameters.

III. COSMOLOGICAL EVOLUTION AND OBSERVATIONAL CONSTRAINTS IN DBI-TYPE K-ESSENCE MODELS

The *Pantheon+SHOES* dataset comprises 1701 light curves corresponding to 1550 distinct Type Ia supernovae (SNe Ia), spanning a redshift range of $z = 0.00122$ to $z = 2.2613$ [74, 75]. The model parameters are constrained by comparing the observed and theoretical values of the distance modulus, which is defined as,

$$\mu(z, \theta) = m - M = 5 \log_{10}(d_l(z)) + 25 \quad (15)$$

where m is apparent magnitude that is how bright object appears from Earth and M is Absolute magnitude that is how bright the object would appear if it were at a standard distance of 10 parsecs and $d_l(z)$ is the dimensionless luminosity distance in Mpc which is defined as [93]:

$$d_l(z) = (1+z)c \int_0^z \frac{dz}{H(z)}. \quad (16)$$

By taking the derivative concerning z we can obtain a differential equation for $d_l(z)$ as:

$$\frac{dd_l(z)}{dz} = \frac{d_l(z)}{1+z} + \frac{c(1+z)}{H(z)} \quad (17)$$

where c is the speed of light measured in unit of km/s .

BAO serves as a powerful probe in contemporary cosmology, enabling precise measurements of the universe's expansion history [94]. Interpreting BAO signatures in large-scale galaxy surveys requires the use of various cosmological distance measures, namely the transverse comoving distance (D_M), the volume-averaged distance (D_V), and the Hubble distance (D_H). These quantities translate angular and redshift separations observed in the sky into physical scales, facilitating the extraction of key cosmological parameters such as the Hubble constant (H_0 , present value) and the dark energy equation of state $\omega(z)$.

In spectroscopic galaxy surveys, the BAO feature manifests both along and across the line of sight. In the radial (line-of-sight) direction, the extent of the BAO peak in redshift space, denoted by a characteristic interval Δz , provides a direct measure of the Hubble parameter via $H(z) = \frac{c\Delta z}{r_d}$ [89, 94–96], where r_d is the comoving sound horizon at the drag epoch. This relation effectively yields the Hubble distance at a given redshift, encapsulating the expansion rate

of the universe at that epoch. Therefore, it measures the Hubble distance at redshift z :

$$D_H(z) = \frac{c}{H(z)}. \quad (18)$$

In the transverse direction, the BAO scale subtends an angle $\Delta\theta$ on the sky, related to the comoving sound horizon r_d through the relation $r_d = D_M(z)\Delta\theta$. By measuring this angular separation at a given redshift, one can infer the comoving angular diameter distance $D_M(z)$, which encapsulates the integrated expansion history of the universe. This distance is expressed as [89, 94–96]:

$$D_M(z) = c(1+z) \int_0^z \frac{dz'}{H(z')}, \quad (19)$$

where $H(z)$ is the Hubble parameter and c is the speed of light. Here, the sound horizon r_d serves as a standard ruler for BAO measurements. It can be expressed as [97, 98]:

$$r_d = \int_{z_{drag}}^{\infty} \frac{c_s}{H(z)} dz. \quad (20)$$

Here, it $z_{drag} \approx 1020$ denotes the baryon drag epoch, the redshift at which baryons decoupled from the photon-baryon plasma. The sound horizon at this epoch, r_d is determined by the sound speed c_s of the photon-baryon fluid prior to decoupling. However, in our analysis, we treat r_d as a free parameter, allowing it to be constrained directly by observational data.

When accounting for the cosmological dependence of r_d , the observables directly constrained by BAO measurements are typically the dimensionless ratios $\frac{D_M(z)}{r_d}$ and $\frac{D_H(z)}{r_d}$. Historically, BAO results have often been encapsulated in a single, spherically averaged distance scale [89, 94–96], defined as:

$$D_V(z) = [z D_M^2(z) D_H(z)]^{1/3}. \quad (21)$$

This isotropic distance measure is especially useful at low redshifts, where the distinction between radial and transverse modes is less pronounced. In such Models, $D_V(z)$ provides a convenient and effective way to capture the combined geometric information from both directions in a single observable.

A. Evolution equation for Model I

To proceed with data analysis employing the total action of the form in Eq. (8), we adopt the specific form of the tension scalar or kinetic coupling factor $f(\phi) = \lambda\phi^4$ and potential $V(\phi) = \frac{m^2\phi^2}{2}$, where λ and m are free, positive, and real parameters [57, 58]. In the framework of k-essence cosmology, the choice of the particular form of $f(\phi)$ ensures the correct DBI dynamics, capturing strong coupling effects and enabling slow-roll inflation via the "D-celeration" mechanism [57]. This kinetic coupling along with the chosen potential $V(\phi)$ plays a crucial role in shaping

the dynamics of the scalar field and its contribution to the background expansion, which may lead to rich cosmological behavior such as transitions from early to late-time accelerated phase [34, 35].

The kinetic coupling factor $f(\phi)$ plays like that of an effective mass in Newton's second law. In classical mechanics, when a particle's mass is position-dependent, its response to applied forces departs from conventional behavior, leading to complex dynamics that are acutely sensitive to the surrounding environment. In our model, it ($f(\phi)$) provides a field-dependent modification to the kinetic energy of the scalar field, thereby functioning as a dynamic "effective mass" term. As the scalar field (ϕ) progresses, this coupling modifies the field's responsiveness to both kinetic and potential components in the action. This results in many dynamical options, enabling the scalar field to either accelerate or decelerate based on its value. The selection of the fourth power of ϕ form for $f(\phi)$ guarantees that minor fluctuations in (ϕ) may induce significant alterations in the field's dynamics, therefore offering an intrinsic mechanism to regulate the speed and characteristics of cosmic evolution.

On the other hand, the quadratic potential $V(\phi) = \frac{m^2\phi^2}{2}$ represents one of the simplest and most well-studied potentials in scalar field cosmology. It introduces a mass scale for the field and supports coherent oscillatory behavior, which can mimic pressure-less matter in certain regimes or drive acceleration in others, depending on the kinetic structure of the theory [100]. When combined with the kinetic coupling, this configuration produces a model that is both analytically tractable and dynamically rich. It supports a wide range of cosmological phenomena, making it an effective framework for studying the interaction of kinetic and potential energy in the evolution of the universe.

Given that the model outlined in Model 1 exhibits intrinsic inconsistencies when seen as a unified scalar field that interpolates between dark matter and dark energy, we reconceptualize the associated Lagrangian (as presented in Eq. (1)) to pertain only to the dark energy sector. To include the matter composition of the universe, we explicitly introduce an additional component to the total Lagrangian (8), representing the matter sector, as detailed in the previous section. Consequently, by integrating both elements, the first and second Friedmann equations may be expressed as:

$$\begin{aligned} 3H^2 &= \rho_m + \rho_\phi \\ &= \rho_m + (\gamma - 1)f(\phi) + V(\phi) \end{aligned} \quad (22)$$

and

$$\begin{aligned} \frac{\ddot{a}}{a} &= -\frac{1}{6}(\rho_m + 3P_m + \rho_\phi + 3P_\phi) \\ &= -\frac{1}{6}(\rho_m + \rho_\phi(1 + 3\omega_{dark})) \end{aligned} \quad (23)$$

where matter sector energy density (ρ_m), and in the dark energy sector, the energy density (ρ_ϕ) satisfy

the following differential equation:

$$\begin{aligned}\frac{d\rho_m}{dt} &= -3H\rho_m \\ \frac{d\rho_\phi}{dt} &= -3H\rho_\phi(1 + \omega_{dark})\end{aligned}\quad (24)$$

where ω_{dark} being defined in Eq. (7). However, we may also define an effective equation of state parameter (ω_{eff}) for this model (Eq. (8)). By defining $\rho_{eff} = \rho_m + \rho_\phi$, $P_{eff} = P_m + P_\phi$ and using Eqs. (22) and (23), ω_{eff} may be expressed in terms of redshift (z) and the Hubble parameter as:

$$\omega_{eff} = -1 - \frac{2}{3} \frac{dH}{H^2} = -1 + \frac{2(1+z)}{3} \frac{dH}{H}. \quad (25)$$

We now define the dimensionless dark energy density parameter (Ω_ϕ) and dimensionless dark matter density parameter (Ω_m) using Eq.(22) as [93]:

$$\Omega_\phi \equiv \Omega_d = \frac{\rho_\phi}{3H^2}; \quad \Omega_m = \frac{\rho_m}{3H^2} \quad (26)$$

the evolution equation for the dark energy density parameter (Ω_d) corresponding to redshift distance (z) can be written as:

$$\frac{d\Omega_d}{dz} = \frac{\Omega_d}{1+z} \left[3(1 + \omega_{dark}) - 2 \frac{(1+z)}{H} \frac{dH}{dz} \right] \quad (27)$$

where we can express $\frac{dH}{dz}$ using Eqs. (22), (23), (24) as:

$$\frac{dH}{dz} = \frac{3H}{2(1+z)} (\Omega_d \omega_{dark} + 1) \quad (28)$$

As observationally redshift distance (z) is the crucial parameter rather than time (t), we must express all equations governing the evolution of Hubble parameter (H), density parameter (Ω_i), scalar field (ϕ), and velocity of scalar field ($\frac{d\phi}{dt}$) in terms of z . Therefore, we can express the scalar field EoM (2) in terms of redshift distance z as:

$$\begin{aligned}\frac{d\phi}{dz} &= \frac{d\phi}{dt} \frac{dt}{dz} = -\frac{v}{H(1+z)} \\ \frac{dv}{dz} &= -\frac{3H}{\gamma^2} \frac{d\phi}{dz} - \frac{3f'(\phi)}{2f(\phi)} \frac{v^2}{H(1+z)} \\ &+ \frac{f'(\phi)}{H(1+z)} \left(1 - \frac{1}{\gamma^3}\right) + \frac{1}{\gamma^3} \frac{V'(\phi)}{H(1+z)},\end{aligned}\quad (29)$$

where we define $\frac{d\phi}{dt} = v$ and $\frac{dz}{dt} = -H(1+z)$.

An important point to emphasize is the distinction between the two equations of state (ω_{dark} and ω_{eff}) used in our analysis. To fit the observational constraints, we employ the definition of the dark energy equation of state parameter, ω_{dark} (7), which directly characterizes the dynamical behavior of the dark energy component. In contrast, the effective equation of state parameter, ω_{eff} (25), is used to describe the overall dynamical behavior of Model I (8), encompassing both dark energy and matter contributions. Once the best-fit parameters are obtained through Bayesian inference and machine learning (ML) techniques, the ω_{eff} serve as a useful tool to interpret the effective cosmological evolution governed by the model.

B. Evolution equations for model II

For the second Model of the DBI-type k-essence model (9), we take the form of the potential coupled to the non-canonical kinetic term as $V(\phi) = \frac{m^2 \phi^2}{2}$, where we again choose m to be a free, positive, and real parameter. The quadratic potential, a simple non-linear potential, is a suitable choice for modeling the dark sector of the universe, offering dynamic behavior and allowing for natural interpolation between relevant regimes. The quadratic-type potential is also a slow-roll-compatible potential in standard inflation [33] and allows analytic progress in the tachyonic-type DBI Model as well [66].

At early times, when the field is evolving rapidly and the kinetic energy dominates, the field behaves effectively like a pressureless fluid. This mimics the characteristics of cold dark matter, thus enabling the scalar field to drive the matter-dominated phase of cosmic evolution. As the field evolves and its velocity decreases, the potential energy begins to dominate. In this regime, the equation of state of the k-essence field approaches that of a cosmological constant, leading to an accelerated expansion akin to dark energy [31, 32].

With the breakdown of the energy density and pressure into their respective components, as specified in Eq. (13), we can derive the first and second Friedmann equations, which are consistent with the Lagrangian presented in Eq. (9) as:

$$3H^2 = \rho_m + \rho_d; \quad \frac{\ddot{a}}{a} = -\frac{1}{6}(\rho_m + 3P_m + \rho_d + 3P_d) \quad (30)$$

Now we define the dimensionless dark energy density parameter (Ω_d) and the dimensionless dark matter density parameter (Ω_m) for Model II as:

$$\Omega_d = \frac{\rho_d}{3H^2}; \quad \Omega_m = \frac{\rho_m}{3H^2} \quad (31)$$

with $\frac{dH}{dz}$ being expressed using Eqs. (11),(12),(14), (30) as:

$$\frac{dH}{dz} = \frac{\sqrt{3\rho_\phi}(1 + \omega_{eff})}{2(1+z)} \quad (32)$$

The evolution equation for dark energy density parameter (31) with respect to redshift distance (z) is expressed as:

$$\frac{d\Omega_d}{dz} = -\frac{2\Omega_d}{H} \frac{dH}{dz} \quad (33)$$

Using the same reasoning as discussed above (before Eq. (29)), we also express the EoM (10) in terms of redshift distance (z) as:

$$\begin{aligned}\frac{d\phi}{dz} &= \frac{d\phi}{dt} \frac{dt}{dz} = -\frac{v}{H(1+z)} \\ \frac{dv}{dz} &= -3\frac{H}{\gamma^2} \frac{d\phi}{dz} + \frac{1}{H(1+z)} \frac{1}{\gamma^2} \frac{V'(\phi)}{V(\phi)}.\end{aligned}\quad (34)$$

In our approach to derive the evolution equations for parameter inference—whether through Bayesian analysis or machine learning methods—we focus on the evolution of the dark energy density parameter, denoted by Ω_d . This choice is made without loss of generality, as it is equally valid to consider the evolution of the dark matter density parameter Ω_m instead. The two parameters are intrinsically linked by the constraint $\Omega_d(z) + \Omega_m(z) = 1$, which holds under the assumption of a spatially flat universe and in the absence of significant contributions from radiation or other exotic components at low redshift. It is worth noting that in principle, a complete energy budget of the universe should include a radiation component characterized by the density parameter Ω_R . However, in the present epoch, the contribution from radiation, comprising photons and relativistic neutrinos, is exceedingly small compared to that of dark matter and dark energy. Owing to the substantial expansion of the universe since the radiation-dominated era, the current value of Ω_R is approximately 10^{-5} [71], rendering its influence negligible in the context of late-time cosmological dynamics. Consequently, we omit the radiation component in our analysis.

Therefore, determining the evolution of either $\Omega_d(z)$ or $\Omega_m(z)$ is sufficient to fully specify the other. In practice, evolving $\Omega_d(z)$ is often more convenient, particularly when exploring dark energy models with dynamic or non-standard equations of state, as the evolution equations can be directly tied to the underlying scalar field dynamics or phenomenological parametrization, as in our case. Once $\Omega_d(z)$ is obtained, the complementary dark matter density parameter follows trivially from the closure relation above.

Another point to mention is that, in the context of scalar field cosmology, particularly for models like DBI-type k-essence ((1) or (8) and (9)), the use of differential equations to determine the evolution of the Hubble parameter $H(z)$, the scalar field $\phi(z)$, its velocity $v(z) = \frac{d\phi}{dt}$, and the density parameter Ω_ϕ or Ω_d , is essential for ensuring a self-consistent and physically accurate description of the dynamics. These quantities are intricately coupled: the evolution of $H(z)$ depends on the energy content of the universe, which in turn is governed by the scalar field dynamics, while $\phi(z)$ and $v(z)$ evolve according to equations that depend explicitly on $H(z)$ and $\gamma(z)$, and the scalar field potential $V(\phi)$. Solving the full set of differential equations allows the system to evolve naturally from initial conditions, preserving the interdependence dictated by the underlying theory. This approach avoids introducing assumptions or approximations that would arise from prescribing analytic forms of $H(z)$ or $\Omega_\phi(z)$, and ensures the model remains valid across the full redshift range. Moreover, in the context of data analysis and parameter inference, evolving the system via differential equations guarantees that predictions are consistently tied to the model parameters, enabling robust comparison with observational data.

IV. METHODOLOGY AND DATA ANALYSIS WITH MODEL FITTING

In this study, we employ a Bayesian statistical framework to infer cosmological parameters of a k-essence model using the NumPyro library [101]. NumPyro is a lightweight probabilistic programming library built on JAX that enables scalable and efficient inference through automatic differentiation and hardware acceleration [102]. The cosmological model is encoded as a probabilistic generative process, where prior distributions are assigned to key parameters such as the present-day dark energy density Ω_{d0} , the Hubble constant H_0 , the scalar field velocity v_0 , and the co-moving sound horizon at the drag epoch r_d . The model's likelihood is defined by comparing theoretical predictions of observables, derived by numerically solving the background dynamics, to the combined datasets from Supernovae (Pantheon+), Hubble measurements, and BAO. Posterior sampling is performed using the No-U-Turn Sampler (NUTS), an adaptive variant of Hamiltonian Monte Carlo (HMC) [60], which allows for efficient exploration of the parameter space even in high dimensions. The resulting chains are analyzed using tools such as ArviZ for diagnostics and GetDist for visualization, yielding robust constraints on the cosmological model parameters.

Machine learning enables the construction of fast and flexible emulators that approximate complex cosmological models by learning from simulated data. In this work, we train a neural network to emulate the evolution of observables, significantly accelerating parameter inference. By comparing the best-fit parameters obtained via machine learning with those from direct ODE integration via Bayesian analysis, we assess the emulator's reliability and precision.

Thereafter, we will also find some functional form of ω_{eff} from the graph of the EoS parameter (ω_{eff}) obtained from the Bayesian method by using gplearn. Gplearn implements symbolic regression using genetic programming (GP) to evolve explicit mathematical expressions that approximate a target function from data. It represents candidate solutions as tree structures composed of basic mathematical operations. It iteratively improves them through genetic operators like mutation, crossover, and selection, optimizing for both model accuracy and complexity.

To conduct the Bayesian analysis, we formulate a five-parameter ($\mathbf{p}=(H_0, \Omega_{d0}, \phi_0, v_0, r_d)$) differential Eqs. (17), (27), (28), (29) concerning the first kind of Lagrangian corresponding to the action (8) and additionally formulate a three-parameter ($\mathbf{p}=(H_0, v_0, r_d)$) differential Eqs. (17), (33), (34) for the second kind of Lagrangian corresponding to the action (9). The solution of these equations with the initial condition is subsequently fitted against the available data set of the type Ia supernova data (*PAN-
THEON+SHOES* data) [74, 75], *Hubble* data [76–88] and for the *BAO* dataset [89–92]. We employ the χ^2 statistics to constrain the model parameters, thereby assessing the discrepancy between the observed data

and a theoretical model. This statistical technique is widely used in hypothesis testing and model fitting to evaluate the adequacy of a model in describing the provided data. For fitting the Bayesian model [60], χ^2 is frequently incorporated into likelihood functions: $L \propto \exp(-\frac{1}{2}\chi^2)$. This establishes a connection between chi-squared minimization and Maximum Likelihood Estimation (MLE), which proves beneficial for Bayesian posterior sampling.

For the model with model parameters (\mathbf{p}), we compute the χ^2 function for the Hubble dataset given in Table VII (*viz.* Appendix) as per [103, 104]:

$$\chi_H^2 = \sum_{i=1}^{43} \left(\frac{H^{th}(z_i, \mathbf{p}) - H^{obs}(z_i)}{\sigma_i} \right)^2 \quad (35)$$

where $H^{th}(z_i, \mathbf{p})$ represents the theoretical value obtained by solving the differential equations, and $H^{obs}(z_i)$ corresponds to the value provided in the $H(z)$ column of Table VII. σ_i denotes the error or uncertainty in the measurement of $H(z)$ as mentioned in the same table.

The χ^2 for BAO data can be computed as [103, 104]:

$$\chi_i^2 = \sum_{i=1}^N \left(\frac{X_i^{th}(z, \mathbf{p}) - X_i^{obs}(z_i)}{\sigma_i} \right)^2, \quad (36)$$

where X_i^{th} is either $\frac{D_M}{r_d}$, $\frac{D_H}{r_d}$, or $\frac{D_V}{r_d}$, calculated theoretically by model fitting. Therefore, the total χ_t^2 corresponding to the BAO dataset is obtained as $\chi_t^2 = \left(\chi_{(\frac{D_M}{r_d})}^2 + \chi_{(\frac{D_V}{r_d})}^2 + \chi_{(\frac{D_H}{r_d})}^2 \right)$.

For the PANTHEON data set corresponding to SN Ia supernovae [74, 75], we employ a different method to obtain χ^2 . This is due to the presence of a covariance matrix (C) of dimension 1701×1701 , which corresponds to the measurement error of the distance modulus ($\mu(z)$) for all 1701 light curves. The expression for χ^2 is as follows:

$$\chi_{SN}^2 = (\mu_{th}(z_i, \mathbf{p}) - \mu_{obs}(z_i))^T C^{-1} (\mu_{th}(z_i, \mathbf{p}) - \mu_{obs}(z_i)) \quad (37)$$

where $\mu_{th}(z_i, \mathbf{p})$ represents the theoretical value derived from Eq. (17) by solving the differential equations specified in Eqs. (27), (28), and (29), corresponds to the first action (1), and also by solving the differential equations specified in Eqs. (32), (33) and (34) correspond to the second action (9), subject to the initial condition and model parameter (\mathbf{p}) as constraints. Here, μ_{obs} denotes the observed value available in the PANTHEON data set [74], and C^{-1} denotes the inverse covariance matrix.

In the machine learning (ML) method [106], to model the cosmological background evolution in a Λ CDM dark energy framework, a deep learning-based

emulator was constructed and calibrated against Pantheon Type Ia supernovae [74, 75], cosmic chronometer Hubble parameter measurements [76–88], and BAO data [89–92]. The coupled evolution equations for the dark energy density (Ω_d), Hubble parameter ($H(z)$), scalar field ($\phi(z)$), and luminosity distance ($d_l(z)$) were solved numerically using “odeint” [105] over a five-dimensional/three-dimensional parameter space ($\mathbf{p}=(H_0, \Omega_{V0}, \phi_0, v_0, r_d)$)/($\mathbf{p}=(H_0, v_0, r_d)$) depending on the action (8) or (9), generating 50,000 (Model I) and 20000 (Model II) (depending on model complexity) realizations of $H(z)$ and $d_l(z)$ across the relevant redshift range. The resulting dataset was standardized and used to train a fully connected neural network comprising two hidden layers with ReLU activation, batch normalization, and dropout regularization, implemented in TensorFlow/Keras [106]. The trained emulator enables rapid and accurate prediction of cosmological observables from model parameters, significantly accelerating likelihood evaluations. Here we also implement the χ^2 statistics and construct the likelihood using the full covariance matrix for Pantheon distances, measurement uncertainties for Hubble data, and BAO-derived quantities $\frac{D_M}{r_d}$, $\frac{D_V}{r_d}$ and $\frac{D_H}{r_d}$, including asymmetric error treatments where required. Parameter estimation was performed in two stages: an initial global search with *Differential Evolution*, followed by local optimization using the L-BFGS-B algorithm [107, 108]. Reproducibility was ensured by fixing random seeds and enforcing deterministic TensorFlow operations. The best-fitting cosmological parameters were obtained and stored for further statistical and physical interpretation. Error estimation has been calculated using the Hessian Matrix method [109–111]. The Hessian matrix is a square matrix of second-order partial derivatives of the loss function with respect to model parameters. In parameter estimation, it characterizes the local curvature of the likelihood surface around the best-fit point. The inverse of the Hessian at this point approximates the covariance matrix of the estimated parameters, allowing one to compute standard deviations as measures of uncertainty. This method assumes a locally Gaussian likelihood and is computationally efficient for estimating errors in ML frameworks.

A. Model I

By performing the Bayesian analysis using NumPyro and ML method, we summarize the optimized best-fit parameter and the corresponding uncertainties in Table I.

Table I presents a side-by-side comparison of cosmological parameter estimates obtained using two distinct statistical frameworks: Machine Learning (ML)-based optimization with uncertainty estimation via the Hessian matrix, and Bayesian inference implemented through NumPyro. While both methods aim to constrain model parameters using observational data, they differ fundamentally in methodology, treat-

Parameter	ML Estimate	ML Std. Dev.	Bayesian Mean	Bayesian Std. Dev.
Ω_{d0}	0.7060	± 0.0140	0.726	± 0.008
H_0	73.4014	± 0.1614	73.638	± 0.16
ϕ_0	2.7866	± 1.8674	2.508	± 0.93
v_0	0.0075	± 0.1111	0.014	$^{+0.019}_{-0.026}$
r_d	139.1689	± 0.6414	139.294	± 0.88

Table I: Comparison of parameter estimates and uncertainties using Machine learning (ML) and Bayesian inference with NumPyro for Model I.

ment of uncertainty, and interpretability. Note that for simplicity we take $\lambda = 1$ and $m = 1$. The rationale for using other values of λ, m is provided in *Appendix B*.

In the ML approach, the parameter values are obtained by minimizing a suitable loss function, using optimization algorithms such as gradient descent and local optimization (L-BGFS-B). Once the best-fit parameters are identified, uncertainties or standard deviation (Std. Dev.) are estimated from the curvature of the loss surface around the optimum using the inverse of the Hessian matrix. This approach assumes that the likelihood surface near the maximum is approximately Gaussian, resulting in symmetric uncertainty (Std. Dev.) intervals. As shown in the table, ML yields relatively narrow and symmetric errors for parameters such as Ω_{d0} , H_0 , and r_d , but exhibits comparatively larger uncertainties for parameters like ϕ_0 and v_0 , possibly reflecting non-Gaussian behavior or weak constraints in those directions.

In contrast, the Bayesian inference framework treats the model parameters as random variables and computes their full posterior distributions by combining prior information with the likelihood function via Bayes' theorem. Using NumPyro, a probabilistic programming library built on JAX, posterior samples are generated using efficient Markov Chain Monte Carlo (MCMC) techniques such as the No-U-Turn Sampler (NUTS), which is used here. The corresponding bayesian plot of the model parameter ($\mathbf{p} = \Omega_{d0}, H_0, \phi_0, v_0, r_d$) is shown in Fig (1) with combined dataset of Pantheon+, Hubble and BAO. This method allows for a more comprehensive exploration of the parameter space, capturing non-Gaussianity, multimodality, and correlations between parameters. For instance, the Bayesian estimate of v_0 includes asymmetric uncertainties ($^{+0.019}_{-0.026}$), highlighting the posterior's skewness, a feature that the Hessian-based ML approach cannot detect. Additionally, the Bayesian uncertainties for parameters such as Ω_{d0} and v_0 are significantly tighter, suggesting that the posterior is better able to exploit the constraining power of the data in those directions.

Overall, while both methods lead to broadly consistent central parameter values, the way they quantify uncertainty is fundamentally different. The ML method provides local approximations around the best-fit point, whereas the Bayesian approach captures the full global structure of the posterior, including any asymmetries or complex dependencies.

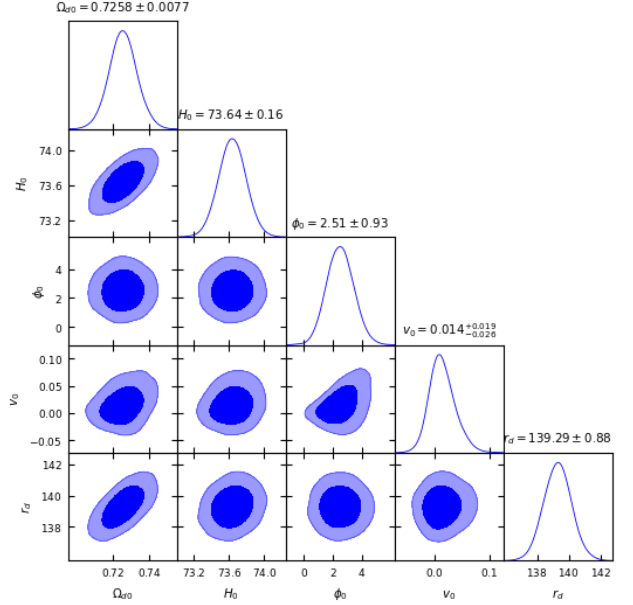


Figure 1: Bayesian Analysis plot for the combined data set of Hubble+ Pantheon+ BAO

B. Model II

For our second model with action (9), we also conduct Bayesian analysis using NumPyro and the ML method to find the optimised best-fit parameter and its uncertainties, which are presented in Table II.

Table II presents a comparative summary of the cosmological parameters derived using two distinct methodologies: a machine learning (ML) emulator approach with Hessian-based uncertainty estimation, and a Bayesian inference framework implemented via NumPyro. Both methods aim to extract best-fit values and credible intervals for key cosmological parameters by incorporating observational constraints from supernovae, Hubble parameter measurements, and BAO data. The resulting central estimates for parameters such as the Hubble constant H_0 , the initial scalar field velocity v_0 , and the sound horizon r_d are in broad agreement between the two approaches, indicating consistency in the underlying data modeling. However, notable differences arise in the estimated uncertainties: the ML-based method yields tighter 1σ confidence intervals, likely reflecting the local curvature information encoded in the Hessian around the best-fit point. In contrast, the Bayesian

Parameter	ML Estimate	ML Std. Dev.	Bayesian Mean	Bayesian Std. Dev.
H_0	75.7814	± 0.1190	75.198	± 0.15
v_0	0.3464	± 0.0051	0.324	± 0.0074
r_d	141.398	± 0.6202	141.643	± 0.90

Table II: Comparison of parameter estimates and uncertainties using Machine learning (ML) and Bayesian inference with NumPyro for Model II.

method explores the full posterior distribution and tends to report wider credible intervals, capturing potential non-Gaussianity and parameter degeneracies more comprehensively. Additionally, the Bayesian framework facilitates marginalization over nuisance parameters and provides direct access to joint and marginalized distributions, offering a richer probabilistic interpretation as it is clearly visible in our Bayesian plot in Fig. (13). These distinctions underscore the complementary strengths of both techniques, ML for efficient parameter estimation in high-dimensional models, and Bayesian inference for a more thorough exploration of parameter space and uncertainty quantification.

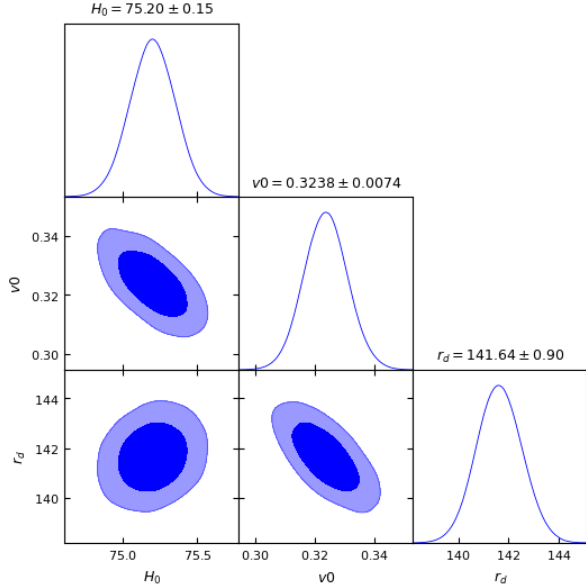


Figure 2: Bayesian Analysis plot for the combined data set of Hubble+ Pantheon+ BAO

Note that, in our analysis, we set the mass parameter $m = 1$. This choice is physically motivated by the fact that the mass parameter appears only through the term $\frac{V'(\phi)}{V(\phi)}$ in our EoM (10). For the chosen quadratic form of the potential, this ratio simplifies to $\frac{V'(\phi)}{V(\phi)} = \frac{2}{\phi}$; ($\phi \neq 0$), which is independent of the mass parameter m . As a result, the scalar field dynamics, and consequently the cosmological evolution encoded in this model, are insensitive to the actual value of m .

This has an important implication for parameter estimation: since m does not affect the background evolution or observables such as luminosity distances or Hubble rates, it cannot be constrained by current background data, including the Pantheon+ super-

nova compilation, BAO measurements (including DES-BAO), or Hubble parameter data. In practical terms, m acts as a degenerate normalization factor in the potential and does not leave any observable imprint on the expansion history. Therefore, the choice of the mass parameter (m) is arbitrary. Thus, we exclude m from the inference analysis and treat it as an unphysical degree of freedom within the context of background-level cosmological constraints.

We also plot the equation of state parameter (ω_{dark} and ω_{eff}) [Eqs. (7), (14) and (25)] with redshift distance (z) for both the model in Fig. 3, Fig.4 and Fig.5 based on Bayesian inference and ML method and reconstruct the functional dependence using symbolic regression technique within the Gplearn framework [112], a genetic programming-based symbolic machine learning technique. This yielded a compact analytical form for model I as:

$$\begin{aligned}\omega_{dark}^{Bayes}(z) &\approx 0.0052z^4 + 0.0042z^3 + 0.00083z^2 - 1 \\ \omega_{dark}^{ML}(z) &\approx 0.00825z^3 - 0.00249z^2 - 1\end{aligned}\quad (38)$$

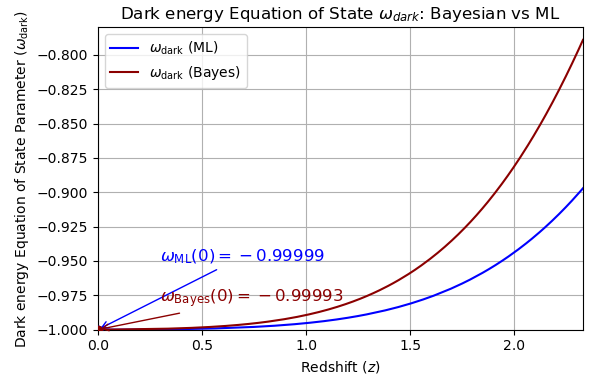


Figure 3: Plot of dark energy EoS parameter (ω_{dark}) with redshift distance (z) for Model I

The plot of the dark energy equation of state parameter, ω_{dark} , as a function of redshift z (Fig.3), reveals a noticeable divergence between the Bayesian and machine learning (ML) approaches, particularly at higher redshifts. This discrepancy arises from differences in parameter inference, specifically, the scalar field ϕ_0 and its velocity v_0 , between the two methods. In the ML-inferred scenario, the scalar field ϕ_0 tends to be larger while its velocity v_0 is smaller compared to the Bayesian estimates. Consequently, the evolution of the kinetic term γ (6), which governs the dynamics of the k-essence field, proceeds more

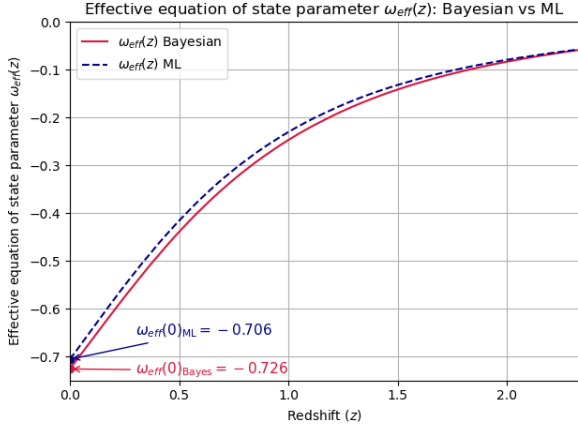


Figure 4: Plot of effective EoS parameter (ω_{eff}) with redshift distance (z) for Model I

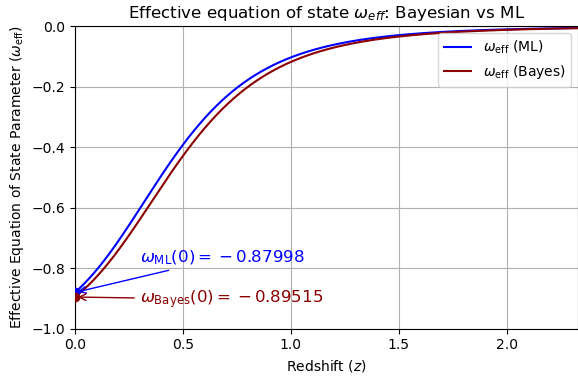


Figure 5: Plot of effective EoS parameter (ω_{eff}) with redshift distance (z) for Model II

slowly in the ML framework. As redshift increases, this slower evolution manifests as an increasingly pronounced deviation in $\omega_{dark}(z)$, which highlights the sensitivity of cosmological dynamics to the underlying inference method. The above expressions

$$\omega_{eff}^{Bayes} = \frac{0.3411z^5 - 0.8201z^4 - 1.0003z^3 - 2.3945z^2 - 2.5104z - 0.6349}{0.4653z^6 + 2.7329z^5 + 6.1018z^4 + 7.4379z^3 + 6.6962z^2 + 4.1836z + 0.874}$$

$$\omega_{eff}^{ML} = -\frac{1.809z^3 + 2.4263z^2 + 0.8184z + 0.2012}{0.6567z^6 + 3.7255z^5 + 5.7006z^4 + 6.3084z^3 + 4.808z^2 + 1.4203z + 0.2836} \quad (39)$$

Note that while the effective equation of state $\omega_{eff}(z)$ remains consistent between the Bayesian and ML inferences (Fig. 4) across the redshift range, the dark energy equation of state $\omega_{dark}(z)$ shows a marked divergence at higher redshifts (Fig. 3). This suggests that although both methods agree on the overall cosmic dynamics (as captured by $\omega_{eff}(z)$), they differ in how they attribute these dynamics to the underlying components. Specifically, the Bayesian inference predicts a more rapidly evolving dark energy behavior, with $\omega_{dark}(z)$ deviating more

reflect a slow evolution of the dark energy EoS from $\omega_{dark}^{Bayes}(z=0) \approx -0.99993$ or $\omega_{dark}^{ML} = -0.99999$, practically indistinguishable from Λ CDM at present time, to $\omega_{dark}^{Bayes}(z) \approx -0.80$ or $\omega_{dark}^{ML} \approx -0.90$ at $z \sim 2.3$. The forms ensure compatibility with both late-time acceleration and structure formation, while allowing for a mild deviation from the cosmological constant at earlier epochs, possibly addressing certain tensions in large-scale structure data (e.g., the σ_8 tension) [73, 113].

In contrast to Λ CDM, which treats the cosmological constant Λ as a fixed energy density with $\omega \approx -1$ [73], our model (model I) introduces a dynamical dark energy component governed by a scalar field whose EoS evolves smoothly with redshift. This evolution, while subtle, offers a possible route to resolving certain observational anomalies and allows exploration of cosmic acceleration *without invoking a fine-tuned vacuum energy* [7].

We also plot the effective equation of state parameter (ω_{eff}) for this model (Model I) using Eq. (25). The plot of the effective EoS ($\omega_{eff}(z)$) is shown in the Fig. (4). Here, both the methods (Bayes and ML) show consistent behavior, with $\omega_{eff}(z)$ rising from negative values at low redshift to nearly zero at higher redshift, indicating a transition from a dark energy-dominated era to a matter-dominated era. At the present epoch ($z = 0$), the Bayesian method yields $\omega_{eff}^{Bayes} = -0.726$ and the ML approach gives $\omega_{eff}^{ML} = -0.706$, both confirming an accelerating universe ($\omega_{eff} < -\frac{1}{3}$) [119]. The close agreement between the two approaches demonstrates the reliability of the ML emulator in capturing cosmological dynamics, while the slight discrepancy highlights the complementary nature of data-driven modeling and statistical inference for constraining dark energy behavior. By using GPlearn we can also find a functional form of ω_{eff} for both the Bayesian and ML methods. The expression is denoted as follows:

significantly from -1 at higher redshifts for the Bayesian method as compared to the ML result. Since $\omega_{eff}(z)$ reflects the combined effect of all energy densities, its agreement between the methods implies that the difference in $\omega_{dark}(z)$ must be compensated by a corresponding adjustment in the dark matter evolution. In other words, the Bayesian model implies a faster decay of dark energy density with redshift, necessitating a greater contribution from dark matter at earlier times to maintain the same overall expansion history. This points to a

fundamental degeneracy in how different components contribute to cosmic acceleration and highlights the sensitivity of dark energy dynamics to the inference method used. Therefore, this DBI-based scalar field model (8) stands as a compelling extension of Λ CDM. It retains all the successful phenomenology of the standard model at low redshift, but opens the door to richer dynamics at higher redshifts.

For Model II, the analytic expression that we found from Fig. (5) using the GPlearn technique [112] is expressed as:

$$\begin{aligned}\omega_{eff}^{Bayes}(z) &\approx -\frac{0.828}{0.65z^5 + 1.235z^4 + 3.326z^3 + z + 0.9} \\ \omega_{eff}^{ML}(z) &\approx \frac{-0.242z + 1.016}{-6z^3 + 0.6z^2 - z - 1.1427}\end{aligned}\quad (40)$$

Based on the plot (Fig. 5) and the GPlearn-derived expression (40) for the effective equation of state $\omega_{eff}(z)$ (Bayesian and ML), the DBI scalar field model (9) with potential $V(\phi) = \frac{m^2\phi^2}{2}$, demonstrates a compelling ability to unify the dark sector. The evolution of $\omega_{eff}(z)$ exhibits a smooth transition from approximately 0 at high redshift, characteristic of pressureless dark matter to dark energy having EoS parameter $\omega_{eff}^{Bayes}(0) = -0.89515$ or $\omega_{eff}^{ML}(0) = -0.87998$ at present, closely approximating the behavior of dark energy. The close agreement between the two curves in Fig.(5) highlights the consistency of the inferred cosmological dynamics. This similarity arises because, in this model, $\omega_{eff}(z)$ depends solely on the parameter v (through $2X = v^2$), and both methods yield nearly identical values for v_0 (as reported in Table II). Consequently, the evolution of $\omega_{eff}(z)$ with redshift follows a nearly identical trajectory in both cases, underscoring the robustness of the model against the choice of inference technique. This behavior, constrained by current observational datasets including Pantheon supernovae, Hubble parameter measurements, and BAO data, indicates that the model not only fits empirical evidence well but also naturally interpolates between the matter-dominated and acceleration-dominated eras of cosmic history. Unlike the standard Λ CDM framework, which invokes two separate components to account for dark matter and dark energy, the DBI model (9) achieves this with a single, dynamically evolving scalar field theory. This unification offers a conceptually elegant and potentially more fundamental alternative to the dual-fluid interpretation of the cosmic dark sector.

Observational data analysis with nuisance parameter μ_0 : To achieve a more accurate and flexible fit to cosmological observations, we introduce a nuisance parameter μ_0 that encapsulates the combined uncertainty in the absolute magnitude (M) of Type Ia supernovae, and H_0 , rather than adopting a fixed offset (commonly taken as 25.15), we absorb these uncertainties into a single additive term μ_0 , which is treated as a free parameter and marginalized over during the inference process. This allows

us to avoid making strong assumptions about the exact values of M or H_0 , focusing instead on the relative luminosity distances constrained by the data [114, 120]. Specifically, we modify Eq. (15) to the following form:

$$\mu(z, \theta) = 5 \log_{10}(d_l(z)) + \mu_0 \quad (41)$$

where the nuisance parameter is given by: $\mu_0 = 25 + 5 \log_{10}(\frac{c}{H_0}) + M$. Here, c is the speed of light in km/s, and M accounts for the absolute magnitude calibration of supernovae. By treating μ_0 as a free parameter in both Bayesian and ML-based analyses, we achieve a model-independent fit that more faithfully reflects the structure of the data.

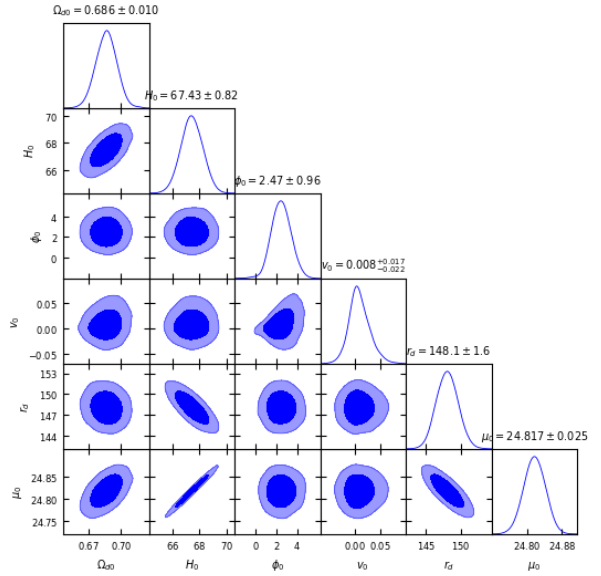


Figure 6: Bayesian Analysis plot for combined dataset of Hubble+ Pantheon+ BAO for Model I with nuisance parameter μ_0

Fig. 6 corresponds to Bayesian analysis of Model I (8) with the nuisance parameter. This results in a six-dimensional parameter space: Ω_{d0} , H_0 , ϕ_0 , v_0 , r_d , μ_0 . The corner plot shows relatively tight posterior constraints with small uncertainties and smooth, nearly Gaussian contours, especially for H_0 and r_d , indicating that the model fits the data well. The inclusion of the nuisance parameter μ_0 slightly broadens the marginalized distributions but helps account for calibration uncertainties. This model displays strong internal consistency and aligns well with observational datasets.

Fig. 7, on the other hand, represents Bayesian analysis for Model II (9). This leads to a simpler four-parameter space: H_0 , v_0 , r_d , μ_0 . The posteriors exhibit broader uncertainties and stronger correlations, particularly between H_0 , v_0 , and μ_0 , suggesting that the model is more sensitive to data and suffers from parameter degeneracies.

The parameter estimates based on ML and Bayesian analysis are listed in Tables (III) and (IV) corresponding to Model I and Model II.

Parameter	ML Estimate	ML Std. Dev.	Bayesian Mean	Bayesian Std. Dev.
Ω_{d0}	0.6933	± 0.056	0.686	± 0.010
H_0	68.8448	± 1.5408	67.43	± 0.82
ϕ_0	2.9676	± 11.9796	2.47	± 0.96
v_0	0.00731	± 0.64320	0.008	$^{+0.017}_{-0.012}$
r_d	148.0876	± 1.0763	148.1	± 1.6
μ_0	24.7973	± 0.0175	24.817	± 0.025

Table III: Comparison of parameter estimates with additional nuisance term (μ_0) and uncertainties using ML and Bayesian inference with NumPyro for Model I.

Parameter	ML Estimate	ML Std. Dev.	Bayesian Mean	Bayesian Std. Dev.
H_0	67.7784	± 0.6171	69.81	± 0.95
v_0	0.4037	± 0.007	0.363	± 0.011
r_d	150.44	± 0.928	148.4	± 1.60
μ_0	24.8098	± 0.0136	24.848	± 0.027

Table IV: Comparison of parameter estimates with additional nuisance term (μ_0) and uncertainties using ML and Bayesian inference with NumPyro for Model II.

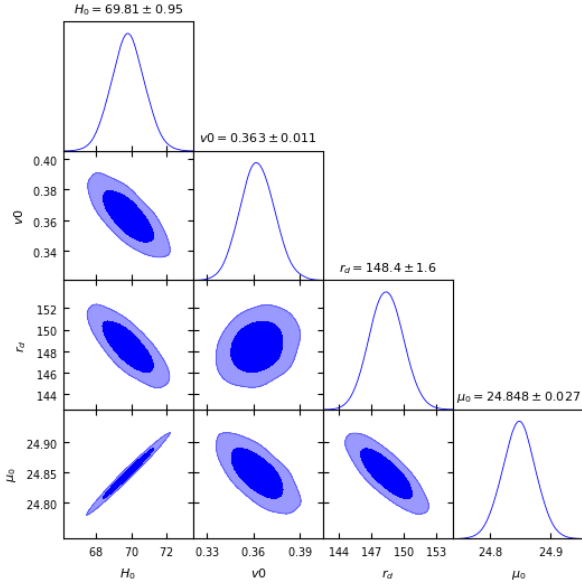


Figure 7: Bayesian Analysis plot for combined dataset of Hubble+ Pantheon+ BAO for Model II with nuisance parameter μ_0

In Model I, Table III, both the ML and Bayesian inference methods yield generally consistent parameter estimates, with Bayesian uncertainties typically smaller and more informative. The Ω_{d0} and H_0 are well constrained in both approaches, though the Bayesian framework yields tighter credible intervals, reflecting better handling of parameter correlations and degeneracies. A significant difference is observed in the uncertainty of the scalar field initial value ϕ_0 , where ML shows a much larger standard deviation (± 11.98) compared to the Bayesian posterior (± 0.96), suggesting that the ML method is less effective in constraining weakly sensitive parameters. The parameter v_0 also displays asymmetric Bayesian uncertainties, indicating a non-Gaussian posterior shape, which ML fails to capture adequately. Overall, the Bayesian approach appears more robust, espe-

cially in the presence of nuisance parameters and degeneracies, providing a more reliable statistical interpretation of the model.

Model II, Table IV, which features a reduced parameter space, shows broadly consistent results between ML and Bayesian methods, though some key differences emerge. The Bayesian estimate $H_0 = 69.81 \pm 0.95$ is noticeably higher than the ML estimate 67.78 ± 0.62 , potentially reflecting sensitivity to prior information or better marginalization over remaining parameters. The parameter v_0 is better constrained in this model compared to Model I, with both methods yielding small uncertainties, although ML again slightly underestimates the error relative to Bayesian inference.

The sound horizon scale r_d and nuisance term μ_0 are consistent across both approaches, with Bayesian uncertainties slightly broader, suggesting more conservative error estimation. These results confirm that Bayesian inference remains more reliable in capturing full posterior structure, especially when dealing with even modest parameter interactions, while ML offers efficient point estimates with limited uncertainty resolution.

V. DISCUSSION

In this section, we discussed a statistical comparison to assess which model best fits the observational data, and we benchmark the results to show how significant our observational analysis via our proposed models is compared to the standard Λ CDM model. Additionally, we compute the deceleration parameter (q) for both models to analyze their cosmological behaviors. Based on our observational data analysis, we construct a summarized table containing statistical criteria as follows:

here,

- χ^2 : Total chi-squared value.
- χ^2_ν : Reduced chi-squared, defined as χ^2/ν ,

Model	Method	χ^2	χ_ν^2	AIC	BIC
Model I	(Bayesian)	1875.9454	1.0629	1885.9454	1913.3391
Model I	(ML)	1876.4491	1.0631	1886.4491	1913.8427
Model II	(Bayesian)	2024.6589	1.1458	2030.6589	2047.0951
Model II	(ML)	1970.1306	1.1149	1976.1306	1992.5668
Λ CDM	(Bayesian)	1871.7476	1.0593	1887.7476	1894.1837
Λ CDM	(ML)	1880.2449	1.0641	1886.2449	1902.6811

Table V: Comparison of statistical criteria for Model I and Model II with Λ CDM using Bayesian and Machine Learning (ML) inference methods

where ν is the number of degrees of freedom, defined as $\nu = N - k$, where N = the number of data points and k = number of model parameters.

- **AIC:** Akaike Information Criterion, defined as $AIC = \chi^2 + 2k$.
- **BIC:** Bayesian Information Criterion, defined as $BIC = \chi^2 + k \ln N$.

In this table V, the number of data points (N) for both the models is the same ($N = 1770$) while the number of model parameters (k) for Models I, Model II and Λ CDM are respectively $k = 5$, $k = 3$ and $k = 3$.

To evaluate and compare the performance of the two proposed models, Model I and Model II against the Λ CDM model, we analyze their statistical metrics: total chi-squared χ^2 , reduced chi-squared χ_ν^2 , AIC, and BIC. These criteria collectively assess the goodness of fit and penalize model complexity, thus enabling a balanced model selection.

Model I yields a lower total chi-squared value ($\chi_{Bayes}^2 = 1875.9454$ or $\chi_{ML}^2 = 1876.4491$) compared to Model II ($\chi_{Bayes}^2 = 2024.6589$ or $\chi_{ML}^2 = 1970.1306$), indicating a better overall fit to the data. The reduced chi-squared values further support this, with $\chi_\nu^2 (Bayes) = 1.0629$ ($\chi_\nu^2 (ML) = 1.0631$) for Model I and $\chi_\nu^2 (Bayes) = 1.1458$ ($\chi_\nu^2 (ML) = 1.1149$) for Model II. Since the reduced chi-squared for Model I is closer to unity, it suggests that this model fits the data within the expected statistical uncertainty, assuming normally distributed residuals.

When considering model selection criteria that include complexity penalties, Model I continues to outperform Model II. The AIC for Model I is $AIC_{Bayes} = 1885.9454$ or $AIC_{ML} = 1886.4491$ versus $AIC_{Bayes} = 2030.6589$ or $AIC_{ML} = 1976.1306$ for Model II. AIC favors models with lower information loss, and a difference of $\Delta AIC > 10$ is generally considered strong evidence against the higher-AIC model—in this case, Model II. Similarly, BIC, which imposes a stronger penalty for model complexity due to its dependence on the number of data points ($N = 1770$), also favors Model I ($BIC_{Bayes} = 1913.3391$ or $BIC_{ML} = 1913.8427$) over Model II ($BIC_{Bayes} = 2047.0951$ or $BIC_{ML} = 1992.5668$). In all statistical parameters, Model I is in close to very good agreement with that of Λ CDM model

(Table(V)), without considering fine tuning and cosmological constant problems.

It is important to note that Model I uses five parameters while Model II uses only three. Despite its greater complexity, Model I achieves significantly better statistical scores, justifying the inclusion of the additional parameters. This suggests that the increased complexity is warranted by a correspondingly improved fit.

In conclusion, under all statistical criteria considered, goodness of fit and information-theoretic model selection metrics, Model I demonstrates a superior performance. The model not only fits the observational data more closely but does so without overfitting, as reflected in its more favorable AIC and BIC values. Thus, in the context of observational cosmological data (Pantheon, Hubble, and BAO), Model I is statistically more viable than Model II.

The worse fit of Model II can be interpreted as a reflection of the inherent limitations of a single-field unified framework to accurately interpolate between dark matter and dark energy behaviors over cosmic time. This highlights both the ambition and the constraint of unification models: *they offer conceptual simplicity at the cost of reduced flexibility, which can translate into statistical tension with precision cosmological data.*

Although Model I is statistically favored over Model II, a more comprehensive judgment requires not only quantitative model comparison but also a physical interpretation of the underlying dynamics. This is achieved by analyzing the behavior of the deceleration parameter ($q = -1 - \frac{dH}{H^2} = -1 + (1+z)\frac{dH}{H}$), which encapsulates the acceleration history of the universe. By estimating the model parameters through observational constraints and subsequently computing the redshift evolution of $q(z)$, we gain deeper insight into the cosmic expansion trends characteristic of each model. The resulting deceleration profiles, presented in Fig. (8) and Fig. (9), visually demonstrate the contrasting acceleration mechanisms. These dynamical insights serve to contextualize the statistical findings within a physically interpretable framework, allowing us to assess not just which model fits best, but why it behaves the way it does.

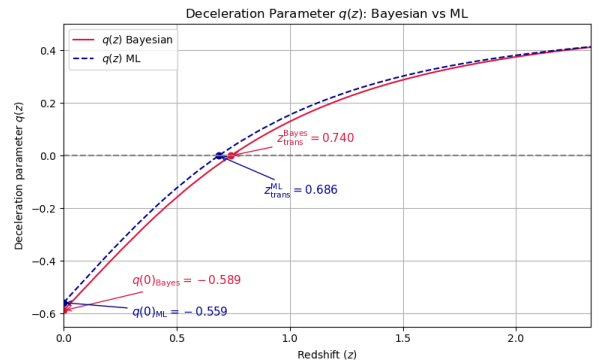


Figure 8: Plot of deceleration parameter (q) with redshift distance (z) for Model I

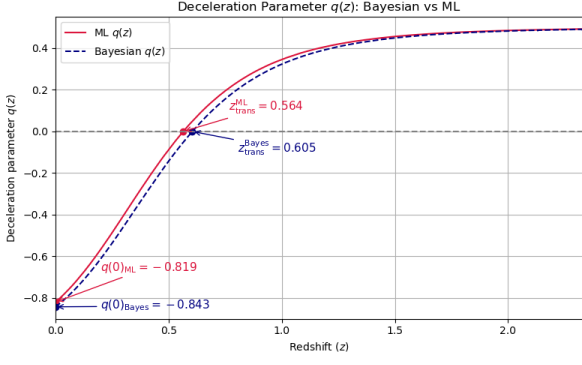


Figure 9: Plot of deceleration parameter (q) with redshift distance(z) for Model II

The comparative analysis of the two k-essence dynamical dark energy models—Model I and Model II, reveals important distinctions in their cosmological behaviors when measured against the benchmark Λ CDM model, which remains the standard paradigm supported by high-precision observations such as Planck CMB data [14], BAO measurements [89], and Type Ia Supernovae [114].

Model I, constructed from a DBI-like k-essence Lagrangian of the form $\mathcal{L} = -f(\phi)\sqrt{1 - \frac{2X}{f(\phi)}} + f(\phi) - V(\phi) + \mathcal{L}_m$ with $f(\phi) = \lambda\phi^4$ and $V(\phi) = \frac{m^2\phi^2}{2}$, predicts a present-day deceleration parameter $q_{\text{Bayes}}(0) = -0.589$ ($q_{\text{ML}}(0) = -0.559$) and a transition redshift $z_{\text{trans}}^{\text{Bayes}} = 0.740$ ($z_{\text{trans}}^{\text{ML}} = 0.686$). These values indicate that cosmic acceleration began relatively early and is proceeding at a rate comparable to Λ CDM, which typically gives $q_{\text{Bayes}}^{\Lambda\text{CDM}}(0) = -0.588$ ($q_{\text{ML}}^{\Lambda\text{CDM}}(0) = -0.572$) and $z_{\text{trans}}^{\text{Bayes}} = 0.742$ ($z_{\text{trans}}^{\text{ML}} = 0.711$) (Appendix Fig. 12) [15, 73]. The Hubble constant $H_0 = 73.64$ (ML inferred value $H_0 = 73.40$) km/s/Mpc and sound horizon $r_d = 139.294$ (ML inferred value $r_d = 139.169$) Mpc inferred in Model I are also consistent with efforts to resolve the Hubble tension, the discrepancy between local measurements (e.g., SH0ES: $H_0 \approx 73$) and early-universe inferences (e.g., Planck: $H_0 \approx 67.4$), while preserving compatibility with BAO and supernova data.

By contrast, Model II, with its simplified DBI-type Lagrangian $\mathcal{L}(\phi, X) = -V(\phi)\sqrt{1 - 2X}$ and the same potential $V(\phi) = \frac{m^2\phi^2}{2}$, yields a significantly stronger acceleration today $q_{\text{Bayes}}(0) = -0.843$ ($q_{\text{ML}}(0) = -0.819$), but with a delayed transition at $z_{\text{trans}}^{\text{Bayes}} = 0.605$ ($z_{\text{trans}}^{\text{ML}} = 0.564$), indicating that dark energy becomes dominant later but with greater intensity. Its much higher dark energy density $\Omega_{d0} = 0.89515$ (see B3), elevated Hubble parameter $H_0 = 75.198$ (ML inferred value $H_0 = 75.7814$) km/s/Mpc, and slightly higher sound horizon $r_d = 141.643$ (ML inferred value $r_d = 141.398$) Mpc are consistent with more aggressive attempts to solve the Hubble tension by introducing significant deviations from Λ CDM at late times [115, 116]. However, such models often come at the cost of tension with early-universe observables, particularly the CMB and early BAO

constraints, which prefer a lower dark energy contribution and earlier acceleration.

Physically, the choice between these models hinges on the assumption of which datasets are considered more fundamental. If one takes Λ CDM as the standard model, supported by Planck and early-time observations, then Model I is clearly the more favorable extension. It maintains a Λ CDM-like evolution of the deceleration parameter, supports a moderately higher H_0 in line with local measurements, and keeps Ω_{d0} and r_d within acceptable shifts that do not overly disrupt early-time fits. Its dynamics are consistent with slowly evolving scalar field models and minimally intrusive modifications to the standard picture.

In contrast, Model II should be considered only if one prioritizes local H_0 measurements and is willing to accept greater deviations from early-time data, which often necessitate additional new physics (e.g., early dark energy, interactions, or modified gravity) to remain viable [117, 118]. Its steep acceleration and high dark energy density suggest a universe dominated by a rapidly growing dark energy component, which may lead to instabilities or tension with structure formation.

On the other hand, the inclusion of the nuisance parameter μ_0 leads to a significant improvement in the model's performance, as evidenced by the reduction in all key statistical criteria including AIC, BIC, χ^2 , and χ^2_ν as shown in Table VI.

Model	Method	χ^2	χ^2_ν	AIC	BIC
Model I	(Bayesian)	1816.9084	1.0300	1828.9084	1861.7809
Model I	(ML)	1820.1563	1.0318	1832.1563	1865.0287
Model II	(Bayesian)	1992.0378	1.128	2000.0378	2021.9528
Model II	(ML)	1893.7138	1.0723	1901.7138	1923.6288
Λ CDM	(Bayesian)	1815.8296	1.0282	1823.8296	1845.7445
Λ CDM	(ML)	1816.6500	1.0287	1824.6500	1846.5649

Table VI: Comparison of statistical criteria for Model I and Model II with Λ CDM using Bayesian and Machine Learning (ML) inference methods with nuisance parameter μ_0

Table VI clearly demonstrates the improvement in model performance due to the inclusion of the nuisance term μ_0 . For all models and methods, the statistical indicators χ^2 , χ^2_ν , AIC, and BIC are systematically lower when the nuisance parameter is included. Specifically, Model I shows a notable reduction in χ^2 and AIC values in both Bayesian and ML approaches, indicating a better fit and greater model parsimony. Similarly, even the Λ CDM baseline benefits slightly from the inclusion of μ_0 , though the improvement is more modest. These results underscore the importance of accounting for such nuisance parameters in cosmological inference, as they can significantly enhance model compatibility with observational data. Also, from Table VI, we may conclude that Model I best fits the standard Λ CDM model with nuisance parameters.

Therefore, when judged through the lens of physical viability and consistency with the standard Λ CDM cosmology, Model I is the preferred model. It serves as a conservative yet flexible dynamical dark energy extension that can reconcile modest late-time deviations (e.g., in H_0) without significantly departing from the well-established early-universe physics.

VI. CONCLUSION

We may conclude that while both of our models can reproduce key features of cosmic expansion and are compatible with current observational datasets (Pantheon+SN Ia, Hubble, and BAO), Model I (8) is statistically and physically favored. It provides a better fit to the data, as demonstrated by lower values of χ^2 , AIC, and BIC, and offers a more Λ CDM-like evolution of the deceleration parameter. Notably, Model I also accommodates a higher (than Λ CDM) Hubble constant (H_0) consistent with local measurements, thus contributing to the mitigation of the Hubble tension.

Model II, while conceptually attractive due to its unifying character, shows limitations in flexibility. Its delayed and stronger acceleration profile, high present-day dark energy density, and statistical under-performance suggest that such single-field unification may come at the cost of tension with precision data, particularly from the early universe. Notably, our inferred sound horizon (r_d) is in close agreement with the latest findings from BAO measurements reported by Liu et al. [121].

In one of our recent study [45], we found that using a non-affine parametrization of the Raychaudhuri equation in a purely kinetic DBI-type k-essence framework ($\mathcal{L}(X) = -\sqrt{1-2X}$) led to a deceleration parameter of $q = -0.58$ and a transition redshift of $z_{trans} = 0.73$. These values imply that the universe began accelerating earlier in its history and that dark energy had a significant influence even at higher redshifts. This points to a scenario where dark energy domination sets in earlier, possibly modifying structure formation and affecting the observable signatures in high-redshift datasets.

In contrast to [45], our present analysis uses the same kinetic structure but with an additional potential term ($V(\phi)$) (Model II) yields $q_{Bayes} = -0.843$ or $q_{ML} = -0.819$ with $z_{trans}^{Bayes} = 0.604$ or $z_{trans}^{ML} = 0.564$. The more negative value of q indicates a stronger present-day acceleration, while the lower transition redshift implies that acceleration began more recently compared to the previous Model. This result is consistent with a scenario where dark energy's influence becomes significant only at lower redshifts, suggesting a steeper late-time evolution of the cosmic expansion.

The shift in z_{trans} to a lower value and the deeper acceleration today make dark energy more dominant only in the recent universe. These distinctions are crucial in determining how viable different k-essence models are in fitting current observational data and in understanding the detailed dynamics of cosmic

acceleration.

For comparison, we have also performed both Bayesian and ML analyses by introducing a nuisance parameter μ_0 , aimed at achieving a better cosmological fit. The results highlight the critical role of this parameter in improving the accuracy of parameter estimation. Notably, the inclusion of μ_0 leads to a significant reduction in the inferred value of H_0 , bringing it closer to early universe measurements from the CMB [14]. In contrast, the analysis without μ_0 yields H_0 values that align more closely with local distance ladder measurements [15]. This divergence is physically significant, as it captures the underlying tension between early and late-time determinations of H_0 , and reflects how different modeling assumptions can shift cosmological inferences. *This behavior reflects the core of the Hubble tension: the dependence of H_0 estimates on calibration assumptions and observational systematics.* The nuisance parameter essentially acts as a buffer for those uncertainties. Its inclusion decouples cosmological inference from local calibration issues, revealing a lower H_0 in better agreement with CMB data. Conversely, excluding μ_0 locks the fit to local calibrations, emphasizing the tension.

Physically, the improved fit obtained through the introduction of the nuisance parameter μ_0 stems from its role in modifying the theoretical distance modulus provided in Eq. (15) to Eq. (41). Here, it μ_0 encapsulates residual uncertainties related to the absolute magnitude of standard candles (e.g. Type Ia supernovae) and calibration systematics. Since M and H_0 are degenerate in the distance modulus, μ_0 effectively absorbs this degeneracy, allowing for more reliable estimation of cosmological parameters like Ω_{d0} , v_0 and especially H_0 . *By marginalizing over μ_0 , we decouple model dependent assumptions from observational systematics, thus enhancing the robustness and physical interpretability of the inferred cosmological constraints.*

Additionally, the inferred values of the sound horizon r_d from both Model I and Model II are also in close agreement with early universe CMB data [14], typically around $r_d \sim 147 - 149$ Mpc, with the inclusion of μ_0 . The strong correlation among H_0 , r_d , and μ_0 suggests that these parameters are jointly constrained by distance measurements and share a common dependence on the expansion history of the universe. Physically, this implies that uncertainties or shifts in the calibration of one (e.g., μ_0 from supernova absolute magnitudes) propagate into the inferred values of the others, such as H_0 and r_d . Since both H_0 , and r_d set the overall distance scale in cosmology and μ_0 reflects calibration offsets in observed luminosity distances, their interplay reflects a fundamental degeneracy between the early and late-universe distance scales. This underlines the importance of marginalizing over μ_0 to disentangle cosmological information from observational systematics and to enable a consistent comparison between low-redshift probes (like SNe Ia) and high-redshift data (such as BAO).

From a methodological perspective, this work demonstrates the complementary power of Bayesian sampling and machine learning based emulators in cosmological model inference. The Bayesian framework captures full posterior distributions and parameter degeneracies, while machine learning accelerates likelihood evaluations, enabling rapid exploration of complex models.

Overall, our findings underscore the potential of DBI-type k-essence models (1) with standard action, particularly the unified variant (Model I (Eq. (8))), as viable dynamical alternatives to Λ CDM. In addition to providing a flexible framework for the late-time acceleration of the universe, Model I also demonstrates the promising capacity to alleviate the Hubble tension. So, we can conclude that among the two models discussed above, Model I (8) provides a better fit to observational data for describing both the early and late-time evolution of the universe. Many more models may exist; however, they are outside the scope of our study. Future extensions incorporating structure formation, non-linear perturbation growth, and updated datasets (e.g., from Euclid, LSST, or JWST) will be crucial in further testing these models (Model I and Model II) and refining our understanding of the dark sector.

Acknowledgement: G.M. extends heartfelt thanks to all the undergraduate, postgraduate, and

doctoral students, as well as to all the teachers, collaborators, and well-wishers, whose support has significantly enriched him. S.G. gratefully acknowledges his father for his unwavering support in shaping his character and guiding his personal growth, and extends sincere appreciation to all co-authors for their valuable and insightful contributions.

Conflicts of interest: The authors declare no conflicts of interest.

Funding information: Not available.

Data availability: The data used in this study are readily accessible from public sources for validation of our model; however, we did not generate any new datasets for this research.

Declaration of competing interest: The authors declare that they have no known competing financial interests or personal relationships that could have appeared to influence the work reported in this paper.

Declaration of generative AI in scientific writing: The authors state that they do not support the use of AI tools to analyze and extract insights from data as part of the study process.

-
- [1] S. Perlmutter et al. ‘Measurements of Ω and Λ from 42 High-Redshift Supernovae’. *The Astrophys. J.*, **517**, 2, 565–86, (1999). <https://doi.org/10.1086/307221>.
 - [2] A.G.Riess et al. ‘Observational Evidence from Supernovae for an Accelerating Universe and a Cosmological Constant’. *The Astronomical J.*, **116**, 3, 1009, (1998). <https://doi.org/10.1086/300499>.
 - [3] M. Tegmark et al. ‘Cosmological Parameters from SDSS and WMAP’. *Phys. Rev. D*, **69**, 10, 103501, (2004). <https://doi.org/10.1103/PhysRevD.69.103501>.
 - [4] D. N. Spergel et al. ‘Three-Year Wilkinson Microwave Anisotropy Probe (WMAP) Observations: Implications for Cosmology’. *The Astrophys. J. Supplement Series*, **170** , 2, 377–408, (2007). <https://doi.org/10.1086/513700>.
 - [5] R. Scranton et al. ‘Physical Evidence for Dark Energy’, (2003). <https://doi.org/10.48550/ARXIV.ASTR0-PH/0307335>.
 - [6] R. Mainini et al. ‘Dark Matter and Dark Energy from a Single Scalar Field and Cosmic Microwave Background Data’. *The Astrophys. J.*, **632**, 2, 691–705, (2005). <https://doi.org/10.1086/433163>.
 - [7] S. Weinberg, ‘The Cosmological Constant Problem’. *Rev. of Mod. Phys.*, **61**, 1, 1–23, (1989). <https://doi.org/10.1103/RevModPhys.61.1>.
 - [8] P.L.E. Peebles, and B. Ratra. ‘The Cosmological Constant and Dark Energy’. *Rev. of Mod. Phys.*, **75**, 2, 559–606, (2003). <https://doi.org/10.1103/RevModPhys.75.559>.
 - [9] T. Padmanabhan, ‘Cosmological Constant—the Weight of the Vacuum’. *Phys. Rep.*, **380**, 5–6, 235–320, (2003). [https://doi.org/10.1016/S0370-1573\(03\)00120-0](https://doi.org/10.1016/S0370-1573(03)00120-0).
 - [10] A. Panda et al., “Cosmological effects on $f(R,T)$ -gravity through a non-standard theory”, *Int. J. Mod. Phys. D* **33**, 03 & 04, 2450015, (2024) <https://doi.org/10.1142/S0218271824500159>
 - [11] A. Panda, D. Gangopadhyay, and G. Manna, “NEC violation in $f(R,T)$ gravity in the context of a non-canonical theory via modified Raychaudhuri equation”, *Astropart. Phys.*, **165**, 103059, (2025). <https://doi.org/10.1016/j.astropartphys.2024.103059>
 - [12] E. V. Linder, “Mapping the cosmological expansion”, *Rept. Prog. Phys.* **71**, 056901, (2008). <https://doi.org/10.1088/0034-4885/71/5/056901>
 - [13] V. Borsevici, S. Ganguly, G. Manna, “Connecting Gravity and Quantum Physics: Primordial Black Holes and Accelerated Evolution of the Universe”, *arXiv:2411.11047*, (2024) <https://doi.org/10.48550/arXiv.2411.11047>
 - [14] Planck Collaboration et al. ‘Planck 2018 Results: VI. Cosmological Parameters’. *A & A*, **641**, A6, <https://doi.org/10.1051/0004-6361/201833910>.
 - [15] A. G. Riess, et al. ‘A Comprehensive Measurement of the Local Value of the Hubble Constant with 1 Km/s/Mpc Uncertainty from the Hubble Space Telescope and the SH0ES Team’. *Astrophys.*

- J. Lett., **934**, 1, L7, (2022). <https://doi.org/10.3847/2041-8213/ac5c5b>.
- [16] B. Ratra, and P. J. E. Peebles. ‘Cosmological Consequences of a Rolling Homogeneous Scalar Field’. Phys. Rev. D, **37**, 12, 3406–27, (1988). <https://doi.org/10.1103/PhysRevD.37.3406>.
- [17] P.G. Ferreira, and M. Joyce. ‘Cosmology with a Primordial Scaling Field’. Phys. Rev. D, **58**, 2, 023503, (1998). <https://doi.org/10.1103/PhysRevD.58.023503>.
- [18] P. Brax, and J. Martin. ‘Quintessence and Supergravity’. Phys. Lett. B, **468**, 1–2, 40–45, (1999). [https://doi.org/10.1016/S0370-2693\(99\)01209-5](https://doi.org/10.1016/S0370-2693(99)01209-5).
- [19] P. Brax, and J. Martin. ‘Robustness of Quintessence’. Phys. Rev. D, **61**, 10, 103502, (2000). <https://doi.org/10.1103/PhysRevD.61.103502>.
- [20] P. Brax, J. Martin, and A. Riazuelo. ‘Exhaustive Study of Cosmic Microwave Background Anisotropies in Quintessential Scenarios’. Phys. Rev. D, **62**, 10, 103505, (2000). <https://doi.org/10.1103/PhysRevD.62.103505>.
- [21] C. Armendariz-Picon, T. Damour, and V. Mukhanov, ‘k-Inflation’, Phys. Lett. B, **458**, 209, (1999). [https://doi.org/10.1016/S0370-2693\(99\)00603-6](https://doi.org/10.1016/S0370-2693(99)00603-6).
- [22] C. Armendariz-Picon, V. Mukhanov, and P. J. Steinhardt, ‘Essentials of k-essence’, Phys. Rev. D, **63**, 103510, (2001). <https://doi.org/10.1103/PhysRevD.63.103510>.
- [23] E. Babichev, V. Mukhanov and A. Vikman, “k-essence, superluminal propagation, causality and emergent geometry”, JHEP, **02**, 101, (2008). <https://doi.org/10.1088/1126-6708/2008/02/101>.
- [24] D. Gangopadhyay, ‘Estimating temperature fluctuations in the early universe’, Gravit. Cosmol., **16**, 231–238, (2010). <https://doi.org/10.1134/S0202289310030072>.
- [25] A. Bandyopadhyay, D. Gangopadhyay, and A. Moulik, “Semiclassical treatment of a k-essence effect on cosmic temperature”, Gravit. Cosmol., **23**, 184–194, (2017). <https://doi.org/10.48550/arXiv.1406.2308>.
- [26] D. Gangopadhyay and S. Mukherjee, “An accelerated universe with negative equation of state parameter in inhomogeneous cosmology with K-essence scalar field”, Phys. Dark Univ., **32**, 100800, (2021). <https://doi.org/10.1016/j.dark.2021.100800>.
- [27] A. Vikman, “K-essence: Cosmology, causality and Emergent Geometry”, Dissertation an der Fakultät für Physik, Arnold Sommerfeld Center for Theoretical Physics, der Ludwig-Maximilians-Universität München, München (2007).
- [28] I. Sawicki, G. Trenkler, A. Vikman, “Causality and Stability from Acoustic Geometry”, arXiv: 2412.21169 (2024), <https://doi.org/10.48550/arXiv.2412.21169>
- [29] L. P. Chimento, “Extended tachyon field, Chaplygin gas, and solvable k-essence cosmologies”, Phys. Rev. D, **69**, 123517, (2004). <https://doi.org/10.1103/PhysRevD.69.123517>.
- [30] M. Visser, C. Barcelo and S. Liberati, “Analogue models of and for gravity”, Gen. Rel. Grav., **34**, 1719–1734, (2002). <https://doi.org/10.1023/A:1020180409214>
- [31] R.J. Scherrer, ‘Purely Kinetic Essence as Unified Dark Matter’, Phys. Rev. Lett., **93**, 011301, (2004). <https://doi.org/10.1103/PhysRevLett.93.011301>.
- [32] T. Padmanabhan and T. Roy Choudhury. ‘Can the Clustered Dark Matter and the Smooth Dark Energy Arise from the Same Scalar Field?’ Phys. Rev. D, **66**, 8, 081301, (2002). <https://doi.org/10.1103/PhysRevD.66.081301>
- [33] V. Mukhanov, Physical foundations of Cosmology, **Cambridge University Press**, New York, (2005).
- [34] C. Armendariz-Picon, et al. ‘Dynamical Solution to the Problem of a Small Cosmological Constant and Late-Time Cosmic Acceleration’. Phys. Rev. Lett., **85**, 21, 4438–41, (2000). <https://doi.org/10.1103/PhysRevLett.85.4438>
- [35] T. Chiba, ‘Tracking k -Essence’. Phys. Rev. D, **66**, 6, 063514, (2002). <https://doi.org/10.1103/PhysRevD.66.063514>
- [36] S. Mukohyama, R. Namba, and Y. Watanabe, “Is the DBI scalar field as fragile as other k-essence fields?”, Phys. Rev. D, **94**, 2, 023514, (2016). <https://doi.org/10.1103/PhysRevD.94.023514>.
- [37] S. Das, A. Panda, G. Manna, S. Ray, ‘Raychaudhuri Equation in K -essence Geometry: Conditional Singular and Non-Singular Cosmological Models’, Fortschr. Phys., **71**, 4-5, 2200193, (2023). <https://doi.org/10.1002/prop.202200193>
- [38] G. Manna, D. Gangopadhyay, “The Hawking temperature in the context of dark energy for Reissner–Nordstrom and Kerr background”, Eur. Phys. J. C, **74**, 2811, (2014). <https://doi.org/10.1140/epjc/s10052-014-2811-9>.
- [39] G. Manna, “Gravitational collapse for the K-essence emergent Vaidya spacetime”, Eur. Phys. J. C, **80**, 9, 813, (2020). <https://doi.org/10.1140/epjc/s10052-020-8383-y>.
- [40] G. Manna, P. Majumdar, and B. Majumder, “K-essence emergent spacetime as a generalized Vaidya geometry”, Phys. Rev. D, **101**, 12, 124034, (2020). <https://doi.org/10.1103/PhysRevD.101.124034>.
- [41] G. Manna, B. Majumder, and A. Das, “Thermodynamics for the k-essence emergent Reissner–Nordstrom–de Sitter spacetime”, Eur. Phys. J. Plus, **135**, 1, 107, (2020). <https://doi.org/10.1140/epjp/s13360-020-00177-2>.
- [42] G. Manna and B. Majumder, “The Hawking temperature in the context of dark energy for Kerr–Newman and Kerr–Newman–AdS backgrounds”, Eur. Phys. J. C, **79**, 7, 553, (2019). <https://doi.org/10.1140/epjc/s10052-019-7066-z>.
- [43] B. Majumder, S. Ray, and G. Manna, “Evaporation of Dynamical Horizon with the Hawking Temperature in the K-essence Emergent Vaidya Spacetime”, Fortschr. Phys., **71**, 10-11, 2300133, (2023). <https://doi.org/10.1002/prop.202300133>.
- [44] B. Majumder, M. Khlopov, S. Ray, and G. Manna, “Geodesic structure of generalized Vaidya spacetime through the K-essence”, Universe, **9**, 12, 510, (2023). <https://doi.org/10.3390/universe9120510>.
- [45] S. Ganguly et. al., “Non-Affine Extensions of the Raychaudhuri Equation in the K-essence Framework”, arXiv:2503.03076, (2025), <https://doi.org/10.48550/arXiv.2503.03076>
- [46] A. Panda, D. Gangopadhyay, G. Manna “Form Invariance of Raychaudhuri equation in the presence of Inflaton-type fields.”, Fortschr. Phys., **72**, 9–10, 2400134, (2024). [doi:10.1002/prop.202400134](https://doi.org/10.1002/prop.202400134).
- [47] A. Panda et al., “Thermodynamics of a Non-

- canonical $f(R, T)$ gravity”, *Phys. Dark Univ.* **46**, 101697, (2024) <https://doi.org/10.1016/j.dark.2024.101697>
- [48] L. García, et al. ‘K-Essence Scalar Field as Dynamical Dark Energy’, (2012). <https://doi.org/10.48550/arXiv.1210.5259>.
- [49] G. W. Horndeski, “Second-order scalar-tensor field equations in a four-dimensional space”, *Int. J. Theor. Phys.* **10**, 363–384 (1974). <https://doi.org/10.1007/BF01807638>
- [50] C. Deffayet et al, “From k-essence to generalised Galileons”, *Phys. Rev. D* **84**, 064039, (2011) <https://doi.org/10.1103/PhysRevD.84.064039>
- [51] A. Joyce et al, “Beyond the Cosmological Standard Model”, *Phys. Rep.*, **568**, 1–98 (2015). <https://doi.org/10.1016/j.physrep.2014.12.002>
- [52] E. Guendelman, R. Herrera and D. Benisty, ‘Unifying inflation with early and late dark energy with multiple fields: Spontaneously broken scale invariant two measures theory’, *Phys. Rev. D*, **105**, 124035, (2022). <http://dx.doi.org/10.1103/PhysRevD.105.124035>.
- [53] E. Guendelman and R. Herrera, “Unification: Emergent universe followed by inflation and dark epochs from multi-field theory”, *Annal. Phys.*, **460**, 169566, (2024). <https://doi.org/10.1016/j.aop.2023.169566>.
- [54] E. I. Guendelman and A. B. Kaganovich. ‘Fine-Tuning Free Paradigm of Two-Measures Theory: K -Essence, Absence of Initial Singularity of the Curvature, and Inflation with Graceful Exit to the Zero Cosmological Constant State’. *Phys. Rev. D*, **75**, 8, 083505, (2007). <https://doi.org/10.1103/PhysRevD.75.083505>.
- [55] M. Born and L. Infeld, ‘Foundations of the New Field Theory’. *Proceed. Royal Soc. London Ser. A*, **144**, 852, 425–51, (1934). <https://doi.org/10.1098/rspa.1934.0059>.
- [56] G. Dvali and S.H. H. Tye, ‘Brane inflation’ , *Phys. Lett. B*, **450**, 1–3, 72–82, (1999). [https://doi.org/10.1016/S0370-2693\(99\)00132-X](https://doi.org/10.1016/S0370-2693(99)00132-X).
- [57] E. Silverstein and D. Tong, ‘Scalar speed limits and cosmology’. *Phys. Rev. D*, **70**, 10, 103505, (2004). <https://doi.org/10.1103/PhysRevD.70.103505>.
- [58] M. Alishahiha, E. Silverstein, and D. Tong, “DBI in the sky: Non-Gaussianity from inflation with a speed limit”. *Phys. Rev. D* **70**, 123505, (2004) <https://doi.org/10.1103/PhysRevD.70.123505>
- [59] E. I. Guendelman, “Dynamical string tension theories with target space scale invariance SSB and restoration”, *Eur. Phys. J. C*, **85**, 276, (2025) <https://doi.org/10.1140/epjc/s10052-025-13966-9>
- [60] M. D. Hoffman and A. Gelman, ‘The No-U-Turn Sampler: Adaptively setting path lengths in Hamiltonian Monte Carlo’, *J. of Machine Learn. Resear.*, **15**, 1593–1623, (2014). <https://arxiv.org/abs/1111.4246>
- [61] M. Ntampaka et al. ‘The Role of Machine Learning in the Next Decade of Cosmology’. (2019). <https://doi.org/10.48550/ARXIV.1902.10159>.
- [62] M. Betancourt, ‘A Conceptual Introduction to Hamiltonian Monte Carlo’. (2017). <https://doi.org/10.48550/ARXIV.1701.02434>.
- [63] A. Gelman et al. (2013). *Bayesian Data Analysis (3rd ed.)*. CRC Press. <https://sites.stat.columbia.edu/gelman/book/BDA3.pdf>
- [64] J. Martin and M. Yamaguchi. ‘DBI-Essence’. *Phys. Rev. D*, **77**, 12, 123508, (2008). <https://doi.org/10.1103/PhysRevD.77.123508>.
- [65] E. J. Copeland et al. ‘DYNAMICS OF DARK ENERGY’. *Int. J. of Mod. Phys. D*, **15**, 11, 1753–935, (2006). <https://doi.org/10.1142/S021827180600942X>.
- [66] A. Sen, ‘Rolling Tachyon’. *JHEP*, **2002**, 04, 048–048, (2002). <https://doi.org/10.1088/1126-6708/2002/04/048>.
- [67] T. Padmanabhan, ‘Accelerated Expansion of the Universe Driven by Tachyonic Matter’. *Phys. Rev. D*, **66**, 2, 021301, (2002). <https://doi.org/10.1103/PhysRevD.66.021301>.
- [68] J.S. Bagla, H.K. Jassal, and T. Padmanabhan, ‘Cosmology with tachyon field as dark energy’, *Phys. Rev. D* **67**, 063504 (2003). <https://doi.org/10.1103/PhysRevD.67.063504>
- [69] P. A. R. Ade et al. (Planck Collaboration), “Planck 2015 results-XIV. dark energy and modified gravity”, *A & A*, **594**, A14, (2016). <https://doi.org/10.1051/0004-6361/201525814>.
- [70] N. Aghanim et al. (Planck Collaboration), ‘Planck 2018 results-VI. Cosmological parameters’, *A & A*, **641**, A6, (2020). <https://doi.org/10.1051/0004-6361/201833910>.
- [71] N. Aghanim et al. (Planck Collaboration), ‘Planck 2018 results. I. Overview and the cosmological legacy of Planck’, *A & A*, **641**, A1, (2020). <https://doi.org/10.1051/0004-6361/201833880>.
- [72] K. Nozari and N. Rashidi, “Mimetic DBI Inflation in Confrontation with Planck2018 data”, *Astrophys. J.*, **882**, 78, (2019) <https://doi.org/10.3847/1538-4357/ab334b>
- [73] P. Pareek and A. Nautiyal, “Reheating constraints on k-inflation”, *Phys. Rev. D* **104**, 083526, (2021), <https://doi.org/10.1103/PhysRevD.104.083526>
- [74] D. Brout et al. “The Pantheon+ Analysis: Cosmological Constraints”. *Astrophys. J.*, **938**, 2, 110, (2022). <http://doi.org/10.3847/1538-4357/ac8e04>
- [75] D. Scolnic et al. ‘The Pantheon+ Analysis: The Full Data Set and Light-Curve Release’. *Astrophys. J.*, **938**, 2, 113, (2022). <https://doi.org/10.3847/1538-4357/ac8b7a>.
- [76] T. M. C. Abbott et al. ‘Dark Energy Survey Year 1 Results: A Precise H_0 Estimate from DES Y1, BAO, and D/H Data’. *MNRAS*, **480**, 3, 3879–88, (2018). <https://doi.org/10.1093/mnras/sty1939>.
- [77] Shadab Alam et al. ‘The Clustering of Galaxies in the Completed SDSS-III Baryon Oscillation Spectroscopic Survey: Cosmological Analysis of the DR12 Galaxy Sample’. *MNRAS*, **470**, 3, 2617–52, (2017). <https://doi.org/10.1093/mnras/stx721>.
- [78] Fotios K. Anagnostopoulos and Spyros Basilakos. ‘Constraining the Dark Energy Models with $H(z)$ Data: An Approach Independent of H_0 ’. *Phys. Rev. D*, **97**, 6, 063503, (2018). <https://doi.org/10.1103/PhysRevD.97.063503>.
- [79] Metin Ata, et al. ‘The Clustering of the SDSS-IV Extended Baryon Oscillation Spectroscopic Survey DR14 Quasar Sample: First Measurement of Baryon Acoustic Oscillations between Redshift 0.8 and 2.2’. *MNRAS*, **473**, 4, 4773–94, (2018). <https://doi.org/10.1093/mnras/stx2630>.
- [80] Éric Aubourg et al. ‘Cosmological Implications of Baryon Acoustic Oscillation Measurements’. *Phys. Rev. D*, **92**, 12, 123516, (2015) <https://doi.org/10.1103/PhysRevD.92.123516>.

- 10.1103/PhysRevD.92.123516.
- [81] Julian E. Bautista et al. ‘Measurement of Baryon Acoustic Oscillation Correlations at $z = 2.3$ with SDSS DR12 Ly α -Forests’. *A & A*, **603**, A12, (2017). <https://doi.org/10.1051/0004-6361/201730533>.
 - [82] M. Betoule et al. ‘Improved Cosmological Constraints from a Joint Analysis of the SDSS-II and SNLS Supernova Samples’. *A & A*, **568**, A22, (2014). <https://doi.org/10.1051/0004-6361/201423413>.
 - [83] F. Beutler et al. ‘The 6dF Galaxy Survey: Baryon Acoustic Oscillations and the Local Hubble Constant: 6dFGS: BAOs and the Local Hubble Constant’. *MNRAS*, **416**, 4, 3017–32, (2011). <https://doi.org/10.1111/j.1365-2966.2011.19250.x>.
 - [84] F. Beutler et al. ‘The Clustering of Galaxies in the Completed SDSS-III Baryon Oscillation Spectroscopic Survey: Anisotropic Galaxy Clustering in Fourier Space’. *MNRAS*, **466**, 2, 60, (2017). <https://doi.org/10.1093/mnras/stw3298>.
 - [85] E. Gaztañaga et al. ‘Clustering of Luminous Red Galaxies - IV. Baryon Acoustic Peak in the Line-of-Sight Direction and a Direct Measurement of $H(z)$ ’. *MNRAS*, **399**, 3, 1663–80, (2009). <https://doi.org/10.1111/j.1365-2966.2009.15405.x>.
 - [86] C. Blake et al. ‘The WiggleZ Dark Energy Survey: Mapping the Distance-Redshift Relation with Baryon Acoustic Oscillations: WiggleZ Survey: BAOs in Redshift Slices’. *MNRAS*, **418**, 3, 1707–24, (2011). <https://doi.org/10.1111/j.1365-2966.2011.19592.x>.
 - [87] X. Xu et al. ‘Measuring DA and H at $Z=0.35$ from the SDSS DR7 LRGs Using Baryon Acoustic Oscillations’. *MNRAS*, **431**, 3, 2834–60, (2013). <https://doi.org/10.1093/mnras/stt379>.
 - [88] L. Samushia et al. ‘The Clustering of Galaxies in the SDSS-III DR9 Baryon Oscillation Spectroscopic Survey: Testing Deviations from Λ and General Relativity Using Anisotropic Clustering of Galaxies’. *MNRAS*, **429**, 2, 1514–28, (2013). <https://doi.org/10.1093/mnras/sts443>.
 - [89] S. Alam et al. ‘Completed SDSS-IV Extended Baryon Oscillation Spectroscopic Survey: Cosmological Implications from Two Decades of Spectroscopic Surveys at the Apache Point Observatory’. *Phys. Rev. D*, **103**, 8, 083533, (2021). <https://doi.org/10.1103/PhysRevD.103.083533>.
 - [90] K. S. Dawson et al. ‘The SDSS-IV extended baryon oscillation spectroscopic survey: overview and early data’, *Astronomical J.*, **151**, 2, 44, (2016). Institute of Physics, <https://doi.org/10.3847/0004-6256/151/2/44>.
 - [91] DESI Collaboration et al. ‘DESI 2024 VI: Cosmological Constraints from the Measurements of Baryon Acoustic Oscillations’. *arXiv*, (2024). <https://doi.org/10.48550/ARXIV.2404.03002>.
 - [92] M.E. Levi et al. ‘The Dark Energy Spectroscopic Instrument (DESI)’. *arXiv:1907.10688*, *arXiv*, (2019). <https://doi.org/10.48550/arXiv.1907.10688>.
 - [93] S. Weinberg, ‘*Cosmology*’. **Oxford university press**, (2008).
 - [94] D.J. Eisenstein et al. ‘Detection of the Baryon Acoustic Peak in the Large-Scale Correlation Function of SDSS Luminous Red Galaxies’. *Astrophys. J.*, **633**, 2, 560–74, (2005). <https://doi.org/10.1086/466512>.
 - [95] W.J. Percival et al. ‘Baryon Acoustic Oscillations in the Sloan Digital Sky Survey Data Release 7 Galaxy Sample’. *MNRAS*, **401**, 4, 2148–68, (2010). <https://doi.org/10.1111/j.1365-2966.2009.15812.x>.
 - [96] C. Blake and K. Glazebrook. ‘Probing Dark Energy Using Baryonic Oscillations in the Galaxy Power Spectrum as a Cosmological Ruler’. *Astrophys. J.*, **594**, 2, 665–73, (2003). <https://doi.org/10.1086/376983>.
 - [97] W. Hu and N. Sugiyama. ‘Small-Scale Cosmological Perturbations: An Analytic Approach’, *Astrophys. J.*, **471**, 2, 542–70, (1996). <https://doi.org/10.1086/177989>.
 - [98] D.J. Eisenstein and W. Hu. ‘Baryonic Features in the Matter Transfer Function’, *Astrophys. J.*, **496**, 2, 605–14, (1998). <https://doi.org/10.1086/305424>.
 - [99] T. Chiba, T.Okabe, and M.Yamaguchi, ‘Kinetically Driven Quintessence’. *Phys. Rev. D*, **62**, 2, 023511, (2002). <https://doi.org/10.1103/PhysRevD.62.023511>.
 - [100] S. Unnikrishnan, V. Sahni, and A. Toporensky ‘Refining Inflation Using Non-Canonical Scalars’. *JCAP*, **2012**, 08, 018–018, (2012). <https://doi.org/10.1088/1475-7516/2012/08/018>.
 - [101] R. Trotta, ‘Bayesian the Sky: Bayesian Inference and Model Selection in Cosmology’. *Contempo. Phys.*, **49**, 2, 71–104, (2008). <https://doi.org/10.1080/00107510802066753>.
 - [102] D. Phan, N. Pradhan, M. Jankowiak. ‘Composable Effects for Flexible and Accelerated Probabilistic Programming in NumPyro’. *arXiv*, (2019). <https://doi.org/10.48550/ARXIV.1912.11554>.
 - [103] D. W. Hogg, et al. *Data Analysis Recipes: Fitting a Model to Data*. *arXiv*, (2010), <https://doi.org/10.48550/ARXIV.1008.4686>.
 - [104] D. W. Hogg and D. Foreman-Mackey, “Data Analysis Recipes: Using Markov Chain Monte Carlo”. *ApJS*, **236**, 11, (2018) <https://doi.org/10.3847/1538-4365/aab76e>.
 - [105] A. Ali et al. ‘Numerical Recipes in Python’. *Zenodo*, (2023). <https://doi.org/10.5281/ZENODO.8371793>.
 - [106] A. Géron, ‘*Hands-on machine learning with Scikit-Learn, Keras, and TensorFlow: Concepts, tools, and techniques to build intelligent systems*’ (3rd ed.). O’Reilly Media, (2022).
 - [107] R. Storn and K. Price, “Differential Evolution – A Simple and Efficient Heuristic for Global Optimization over Continuous Spaces,” *Jour. of Global Optimization*, **11**, 4, 341–359, (1997). <https://doi.org/10.1023/A:1008202821328>.
 - [108] C. Zhu, R. H. Byrd, P. Lu, and J. Nocedal, ‘Algorithm 778: L-BFGS-B: Fortran Subroutines for Large-Scale Bound-Constrained Optimization’, *ACM TOMS*, **23**, 4, 550–60, (1997). <https://doi.org/10.1145/279232.279236>.
 - [109] D. R. Cox, and D. V. Hinkley. ‘Theoretical Statistics’. 1st ed., Chapman and Hall/CRC, (1979). <https://doi.org/10.1201/b14832>.
 - [110] C. Bishop, ‘Pattern recognition and machine learning’ (Vol. 4) Ch.7. Springer, (New York), (2006).
 - [111] W. H. Press, and S. A. Teukolsky, and W. T. Vetterling, and Flannery, ‘Numerical Recipes: The Art of Scientific Computing’. Cambridge University Press, (New York), (2007). <http://dx.doi.org/10.1142/S0218196799000199>.
 - [112] S. Meier, ‘gplearn: Genetic Programming in Python’, (2016), <https://github.com/>

- trevorstephens/gplearn
- [113] E. Di Valentino et al. ‘Snowmass2021 - Letter of Interest Cosmology Intertwined I: Perspectives for the next Decade.’ *Astropart. Phys.*, **131**, 102606, (2021). <https://doi.org/10.1016/j.astropartphys.2021.102606>.
- [114] D. M. Scolnic et al. ‘The Complete Light-Curve Sample of Spectroscopically Confirmed SNe Ia from Pan-STARRS1 and Cosmological Constraints from the Combined Pantheon Sample’. *The Astrophys. J.*, **859**, 2, 101, (2018). <https://doi.org/10.3847/1538-4357/aab9bb>.
- [115] E. Di Valentino et al. ‘Snowmass2021 - Letter of Interest Cosmology Intertwined II: The Hubble Constant Tension’. *Astropart. Phys.*, **131**, 102605, (2021). <https://doi.org/10.1016/j.astropartphys.2021.102605>.
- [116] V. Poulin et al. ‘Early Dark Energy Can Resolve the Hubble Tension’. *Phys. Rev. Lett.*, **122**, 22, 221301, (2019). <https://doi.org/10.1103/PhysRevLett.122.221301>.
- [117] J. C. Hill et al. ‘Early Dark Energy Does Not Restore Cosmological Concordance’. *Phys. Rev. D*, **102**, 4, 043507, (2020). <https://doi.org/10.1103/PhysRevD.102.043507>.
- [118] L. Knox and M. Millea. ‘Hubble Constant Hunter’s Guide’. *Phys. Rev. D*, **101**, 4, 043533, (2020). <https://doi.org/10.1103/PhysRevD.101.043533>.
- [119] P. J. E. Peebles, ‘Principles of physical cosmology’, **Princeton: Princeton University Press** (1993).
- [120] A. Conley et al. ‘Supernova constraints and systematic uncertainties from the first three years of the supernova legacy survey’, *Astrophys. J. Suppl. Ser.*, **192**, 1, p. 1, (2011). <https://doi.org/10.1088/0067-0049/192/1/1>.
- [121] T. Liu, S. Cao, J. Wang, ‘Model-Independent Determination of the Sound Horizon Using Recent BAO Measurements and Strong Lensing Systems’. *Phys. Rev. D*, **111**, 2, 023524, (2025). <https://doi.org/10.1103/PhysRevD.111.023524>.

Appendix A: Hubble and BAO data set

The Hubble parameter measurements $H(z)$ presented in Table VII are compiled from a range of observational studies spanning redshifts from $z \sim 0.7$ to $z \sim 2.36$. These data are derived using two primary techniques: the cosmic chronometer (or differential age) method, denoted by ‘a’, which estimates $H(z)$ by measuring the age difference of passively evolving galaxies at different redshifts; and the baryon acoustic oscillation (BAO) method, denoted by ‘b’, which infers $H(z)$ from the characteristic scale imprinted by sound waves in the early universe. Together, these complementary measurements provide valuable constraints on the cosmic expansion history and are instrumental in testing cosmological models.

There are two BAO datasets that we are going to analyze. The first one contains 8 data points from Sloan Digital Sky Survey (SDSS) [89, 90] called SDSSBAO and the second set contains 7 data points from Dark Energy Spectroscopic Instrument (DESI) [91, 92] called DESBAO. We call the combined dataset (SDSSBAO and DESBAO) as BAO data. These data sets are comprehensively tabulated in

z	$H(z)$	σ_H	Method	Ref.
0.0708	69.0	± 19.68	a	[76]
0.09	69.0	± 12.0	a	[77]
0.12	68.6	± 26.2	a	[76]
0.17	83.0	± 8.0	a	[77]
0.179	75.0	± 4.0	a	[78]
0.199	75.0	± 5.0	a	[78]
0.2	72.9	± 29.6	a	[76]
0.240	79.69	± 2.65	b	[85]
0.27	77.0	± 14.0	a	[77]
0.28	88.8	± 36.6	a	[76]
0.35	84.4	± 7.0	b	[87]
0.352	83.0	± 14.0	a	[78]
0.38	81.2	± 2.2	a	[79]
0.3802	83.0	± 14.0	a	[80]
0.4	95	± 17.0	a	[77]
0.4004	77.0	± 10.2	a	[80]
0.4247	87.1	± 11.2	a	[80]
0.43	86.45	± 3.68	b	[85]
0.44	82.6	± 7.8	b	[86]
0.4497	92.8	± 12.9	a	[80]
0.47	89	± 50	a	[81]
0.4783	80.9	± 9.0	a	[80]
0.48	97.0	± 62.0	a	[81]
0.51	90.90	± 2.1	a	[79]
0.57	92.4	± 4.5	b	[88]
0.593	104.0	± 13.0	a	[78]
0.6	87.9	± 6.1	b	[86]
0.61	98.96	± 2.2	a	[79]
0.68	92.0	± 8.0	a	[78]
0.73	97.3	± 7.0	b	[86]
0.781	105.0	± 12.0	a	[78]
0.875	125.0	± 17.0	a	[78]
0.88	90.0	± 40.0	a	[81]
0.9	117.0	± 23.0	a	[77]
1.037	154.0	± 20.0	a	[78]
1.3	168.0	± 17.0	a	[77]
1.363	160.0	± 33.6	a	[82]
1.43	177.0	± 18.0	a	[77]
1.53	140.0	± 14.0	a	[77]
1.75	202.0	± 40.0	a	[77]
1.965	186.5	± 50.4	a	[82]
2.34	222.0	± 7.0	b	[83]
2.36	226.0	± 8.0	b	[84]

Table VII: Here the unit of $H(z)$ is $km s^{-1} Mpc^{-1}$ ‘a’ quoted in this table means the $H(z)$ value is deduced from cosmic chronological method/differential age method whereas ‘b’ corresponds to that obtained from BAO data and the corresponding reference from where the data are collected is mentioned in the References

Table VIII and Table IX.

Appendix B: Choice of parameter for Model I and Model II

We select a five-parameter ($\mathbf{p}=(H_0, \Omega_{d0}, \phi_0, v_0, r_d)$) differential equation for Model I while restricting the parameters to three ($\mathbf{p}=(H_0, v_0, r_d)$) for Model II. Our choice is solely based on the model’s complexity and the redundancy of additional parameters that have minimal or no impact on the observational

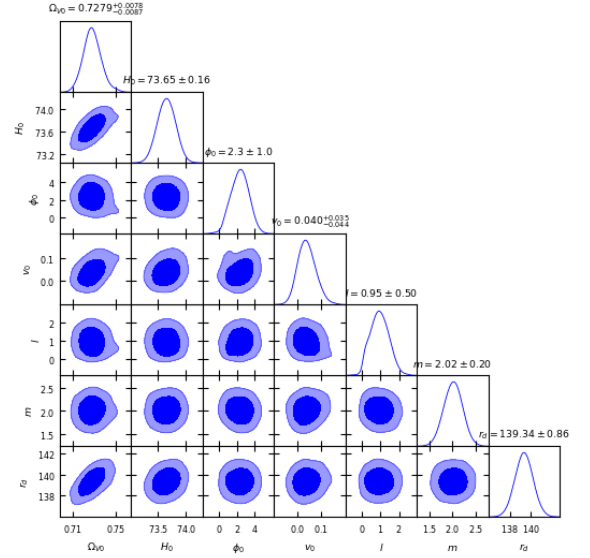
\tilde{z}	0.15	0.38	0.51	0.70	0.85	1.48	2.33	2.33
$D_V(\tilde{z})/r_d$	4.47 ± 0.17				$18.33^{+0.57}_{-0.62}$			
$D_M(\tilde{z})/r_d$		10.23 ± 0.17	13.36 ± 0.21	17.86 ± 0.33		30.69 ± 0.80	37.6 ± 1.9	37.3 ± 1.7
$D_H(\tilde{z})/r_d$		25.00 ± 0.76	22.33 ± 0.58	19.33 ± 0.53		13.26 ± 0.55	8.93 ± 0.28	9.08 ± 0.34

Table VIII: SDSSBAO measurements

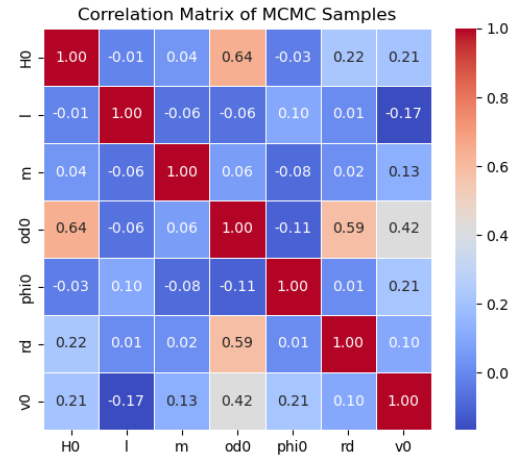
\tilde{z}	0.295	0.510	0.706	0.930	1.317	1.491	2.330
$D_V(\tilde{z})/r_d$	7.93 ± 0.15					26.07 ± 0.67	
$D_M(\tilde{z})/r_d$		13.62 ± 0.25	16.85 ± 0.32	21.71 ± 0.28	27.79 ± 0.69		39.71 ± 0.94
$D_H(\tilde{z})/r_d$		20.98 ± 0.61	20.08 ± 0.60	17.88 ± 0.35	13.82 ± 0.42		8.52 ± 0.17

Table IX: DESBAO measurements

model fitting. In our initial model (Model I), we can choose m and λ as parameters, but we choose not to do so because they do not constrain our model. This can be inferred from the Bayesian plot and the corresponding heatmap (Fig. 10) that represents the correlation between different parameters. In Figure (Fig. 10b), we display the correlation matrix where we select m and λ as additional model parameters along with $(\mathbf{p}=(H_0, \Omega_{V0}, \phi_0, v_0, r_d))$. The initial condition is chosen to be Gaussian, with m having a mean of $\mu_m = 2$ and a standard deviation of $\sigma_m = 0.2$, and λ having a mean of $\mu_\lambda = 1$ and a standard deviation of $\sigma_\lambda = 0.5$.

(a) Bayesian plot for parameter estimation with m and (λ) for Model I

According to the above-presented diagram (Fig. 10), the parameters m and λ exhibit negligible correlation with the other cosmological parameters, as seen in both the Bayesian posterior plot and the heatmap correlation matrix. The corresponding scatter plots show a lack of structured dependence, and the Pearson correlation coefficients are close to zero. This statistical independence suggests that m and λ do not significantly influence the behavior of key observables governed by parameters like H_0 and Ω_{d0} . Therefore, m & λ can be effectively treated as auxiliary or external parameters in the model, and may be fixed to constant values without compromising the accuracy or flexibility of the parameter estimation framework. This simplification can help reduce computational complexity while maintaining model fidelity. Therefore, we restrict ourselves to choosing only five parameters for Model I, and for simplicity, we choose $m = 1$ and $\lambda = 1$.



(b) Heatmap correlation matrix for Model I

Figure 10: Bayesian inference and correlation structure for Model I.

In our first model (Model I), the present-day dark energy density parameter Ω_{d0} is introduced explicitly as a free parameter. However, in the second model, we consider a unified scalar field Lagrangian that simultaneously accounts for both dark energy and dark matter components. In this framework, the scalar field is solely responsible for the entire dark sector. This unification naturally renders Ω_{d0} a derived quantity rather than a fundamental input parameter. This can also be verified from Eq. (30) where we have,

$$3H^2 = \rho_m + \rho_d \quad (\text{B1})$$

with $\rho_m = \frac{V(\phi)2X}{\sqrt{1-2X}}$ and $\rho_d = V(\phi)\sqrt{1-2X}$. Adding these two together, we get,

$$3H^2 = \frac{V(\phi)}{\sqrt{1-2X}} \quad (\text{B2})$$

Therefore, we can write the dark energy and dark matter density parameter as:

$$\Omega_d = \frac{\rho_d}{3H^2} = 1 - 2X ; \Omega_m = \frac{\rho_m}{3H^2} = 2X. \quad (\text{B3})$$

Thus, the evolution and present-day value of Ω_{d0} are not independent but are fully determined by the scalar field dynamics through the kinetic term $X = v^2$. Since Ω_{d0} can be computed from the model equations themselves, it is redundant to treat it as a free parameter. This approach not only simplifies the parameter space but also strengthens the physical consistency of the unified scalar field model. The initial value of the scalar field ϕ can also be inferred from the above Eq.(B2). If we put the value of $V(\phi) = \frac{m^2\phi^2}{2}$ with $m = 1$ in Eq.(B2) then in terms of present day value of Hubble parameter (H_0) and the velocity of scalar field (v_0) (where $X = \frac{v^2}{2}$) we can write:

$$\phi_0 = 6H_0^2 \sqrt{1 - v_0^2} \quad (\text{B4})$$

Therefore, ϕ_0 can also be omitted as a model parameter, and the second model (Model II) effectively reduces to a three-parameter system, enhancing both interpretability and computational efficiency.

Appendix C: Λ CDM Model

We consider the usual Λ CDM model and perform a Bayesian analysis to compare it with two of our proposed models (Model I 8 and Model II 9) under consideration against the combined dataset of Pantheon+, Hubble, and BAO. In this model (Λ CDM), the energy content of the universe is assumed to be dominated by two components: pressureless cold dark matter with energy density ρ_m , and dark energy represented by a cosmological constant Λ , with energy density ρ_d .

Assuming a spatially flat FLRW background, the dynamics of the universe are governed by the Friedmann equations:

$$H^2 = \rho_m + \rho_d \quad (\text{C1})$$

$$\frac{\ddot{a}}{a} = -\frac{1}{6}(\rho_m + 3P_m + \rho_d + 3P_d) \quad (\text{C2})$$

The energy densities satisfy the continuity equation as follows:

$$\begin{aligned} \frac{d\rho_m}{dt} &= -3H\rho_m \\ \frac{d\rho_d}{dt} &= 0. \end{aligned} \quad (\text{C3})$$

We define (Ω_d) and (Ω_m) as $\Omega_d = \frac{\rho_d}{3H^2}$, and $\Omega_m = \frac{\rho_m}{3H^2}$ respectively. These lead to the differential equation for H and Ω_d as,

$$\frac{dH}{dz} = \frac{3H}{2(1+z)}\Omega_m \quad (\text{C4})$$

$$\frac{d\Omega_d}{dz} = -\frac{2\Omega_d}{H} \frac{dH}{dz} \quad (\text{C5})$$

Together with Eq. (C5), the condition $\Omega_m + \Omega_d = 1$ specifies the total energy content of a spatially flat universe.

The set of Eqs. (C4), (C5), (17) along with the condition $\Omega_m + \Omega_d = 1$, allows us to fully determine the evolution of the Hubble parameter and the energy content of the universe.

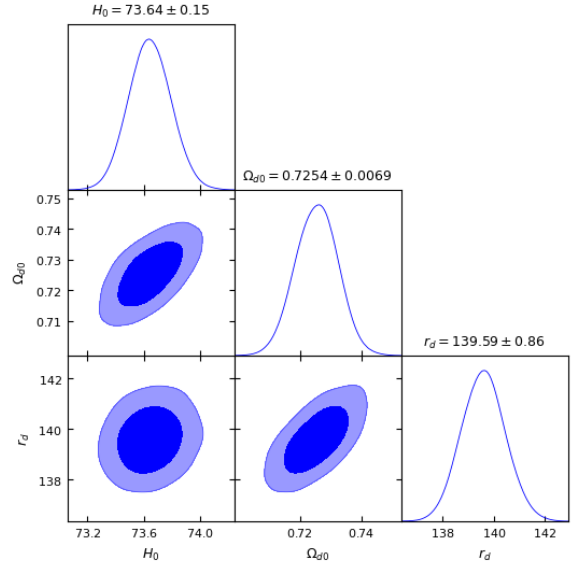


Figure 11: Bayesian Analysis plot for the combined data set of Hubble+ Pantheon+ BAO for Λ CDM Model

For convenience we also plot the declaration parameter q with respect to z for Λ CDM model

Parameter	ML Estimate	ML Std. Dev.	Bayesian Mean	Bayesian Std. Dev.
H_0	73.604	± 0.0909	73.64	± 0.15
Ω_{d0}	0.7086	± 0.0055	0.7254	± 0.0069
r_d	139.1273	± 0.6294	139.59	± 0.86

Table X: Comparison of parameter estimates and uncertainties using Machine learning (ML) and Bayesian inference with NumPyro for Λ CDM Model.

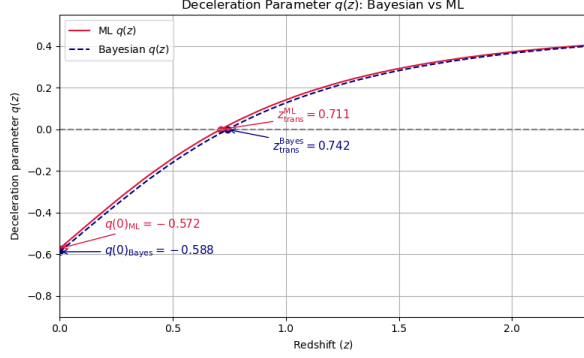


Figure 12: Plot of declaration parameter(q) vs redshift distance(z) for Λ CDM Model

With inclusion of nuisance parameter μ_0 we rerun the Bayesian and ML analysis to get best fit parameters and the corresponding uncertainties as noted down in Table(XI)

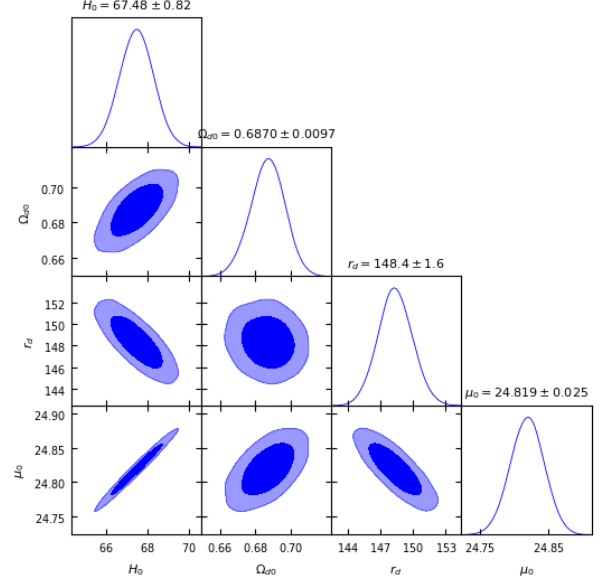


Figure 13: Plot of declaration parameter(q) vs redshift distance(z) for Λ CDM Model with nuisance parameter(μ_0)

Parameter	ML Estimate	ML Std. Dev.	Bayesian Mean	Bayesian Std. Dev.
H_0	67.443	± 0.5431	67.48	± 0.82
Ω_{d0}	0.6781	± 0.0062	0.687	± 0.0097
r_d	149.4481	± 1.1718	148.4	± 1.6
μ_0	24.7849	± 0.0186	24.819	± 0.025

Table XI: Comparison of parameter estimates and uncertainties using Machine learning (ML) and Bayesian inference with NumPyro for Λ CDM Model with nuisance parameter(μ_0).